Progressive failure mechanisms of geosynthetic-reinforced column-supported embankments over soft soil

Numerical analyses considering the cracks-induced softening

Wang, Heng; Chen, Feng; Shiau, Jim; Dias, Daniel; Lai, Fengwen; Huang, Jianhua

DOI
10.1016/j.engstruct.2023.117425

Publication date
2023

Document Version
Final published version

Published in
Engineering Structures

Engineering Structures 302 (2024) 117425

Contents lists available at ScienceDirect

Engineering Structures

journal homepage: www.elsevier.com/locate/engstruct

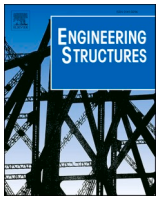

Progressive failure mechanisms of geosynthetic-reinforced column-supported embankments over soft soil: Numerical analyses considering the cracks-induced softening

Heng Wang [a,b], Feng Chen [a], Jim Shiau [c], Daniel Dias [d], Fengwen Lai [e,f,*], Jianhua Huang [a]

[a] Fujian Provincial Key Laboratory of Underground Engineering, School of Civil Engineering, Fujian University of Technology, Fuzhou 350118, China
[b] CSCEC Strait Construction and Development CO., Ltd, Fuzhou 350015, China
[c] School of Engineering, University of Southern Queensland, QLD 4350, Australia
[d] Laboratory 3SR, Grenoble INP, CNRS, Grenoble Alpes University, Grenoble 38000, France
[e] College of Civil Engineering, Fuzhou University, Fuzhou 350108, China
[f] Faculty of Civil Engineering and Geosciences, Delft University of Technology, Delft 2628 CN, the Netherlands

ARTICLE INFO

Keywords:
Geosynthetic-reinforced column-supported embankment
Progressive failure mechanism
Finite element analysis
Strain-softening
Crack

ABSTRACT

Cement-based columns in combination with geosynthetic reinforcement is a well-established soft ground improvement technique to enhance embankment stability. This paper aims to present a finite-element (FE) study based on a case history of a geosynthetic-reinforced column-supported (GRCS) embankment over soft soil. In this study, the columns are simulated with an advanced Concrete model to simulate the development of possible cracking and induced strain-softening. Numerical results are compared against published centrifuge tests, giving confidence to the established FE model with the Concrete model. New insights into the progressive failure mechanisms of GRCS embankments over soft soil are then discussed by examining the stress paths, internal forces, and cracks, as well as the plastic failure zones of columns. In addition, the role of columns and geosynthetics on the progressive failure mechanisms (failure loads and sequences) is also examined by an extensive parametric study. The results suggest that provided the optimization of compressive and tensile forces in the columns combined with the tensile stiffness of the geosynthetics is put in place, more columns can be mobilized to resist global sliding failure and to improve the bearing capacity of GRCS embankments.

1. Introduction

The use of geosynthetic reinforcement at the base of highway or road embankments which are supported by columns/piles is known as geosynthetic-reinforced column-supported (GRCS) embankments. It has been proven as an effective and economical solution in soft soil [10,37,48,51]. There have been different types of columns currently used in GRCS embankments such as stone and cement-based columns (mixing or jet-grouting). Among them, deep cement mixing (DCM) column-supported embankments have increasingly expanded worldwide [21,27,40,46], as it has the following advantages: (a) stronger stability and smaller settlement; (b) rapid construction; (c) reduced cost; (d) minor environmental impact, and (e) construction in complex ground conditions (particularly in deep soft soil). It is well known that progressive failure would be triggered and developed in GRCS embankments as flexible or semi-rigid column/pile-supported systems subjected to additional loadings [22,48,51]. Although extensive evidence [26,28,52] has indicated that the resistance to the instability of GRCS embankments can be provided by a combination of the soil arching effect between columns and the membrane effect of geosynthetic, the role of column and geosynthetics on the progressive mechanisms is still not yet well studied.

Recently, several laboratory tests such as 1 *g* model tests [43,44] and *ng* centrifuge tests [42,47,48] have been carried out to observe the underlying failure mechanisms as well as to assess the stability of GRCS embankments. Due to the design complexities of testing apparatus and the high costs required, experimental investigations are limited for an in-depth interpretation of progressive failure mechanisms. As a consequence, the majority of the existing design procedures, e.g., limit equilibrium ([4]; Van [36]) and limit analysis [18,19,5], were developed based on an assumed global failure of GRCS embankments, where the columns or geosynthetics and the critical slip surfaces coincide. These

* Corresponding author at: College of Civil Engineering, Fuzhou University, Fuzhou 350108, China.
E-mail addresses: F.Lai-1@tudelft.nl, laifengwen@fzu.edu.cn (F. Lai).

https://doi.org/10.1016/j.engstruct.2023.117425
Received 17 August 2023; Received in revised form 25 November 2023; Accepted 21 December 2023
Available online 30 December 2023

methods may result in an over-conservative design.

Numerical modeling has proven to be a powerful tool that can be used to study the (progressive) failure mechanisms of GRCS embankments. Some of the representative numerical methods such as the finite element method (FEM) [17,35,52,53], finite difference method (FDM) [13,14], or discrete element method (DEM) [6,18] were developed to a stage in which the working performance and/or failure mechanisms of GRCS embankments can be well studied. These methods do not need a priori definition of the slip surface and therefore their solutions are accurate, particularly for the prediction of failure modes. They remove the requirement for a priori definition of the slip surface and therefore they do not need to predetermine the failure mode. The emphasis of this paper is put on understanding the progressive failure mechanisms of GRCS embankments on a macro-scale, rather than on a micro-scale. Therefore, the use of the DEM is very time-consuming and unsuitable in this study. The present study uses the FEM to investigate the progressive failure mechanisms of GRCS embankments.

Simple elastic-perfectly plastic failure criteria such as the Mohr-Coulomb (MC) model are frequently employed for modeling cement-based columns supporting embankments, although other advanced models have been developed [22,51]. The columns are generally not reinforced and hence relatively brittle, albeit in some cases a steel bar is immediately placed at the center of the columns after construction to enhance the strength. It is, therefore, desirable to develop an available criterion with the limited tensile strength of such columns. It is also desirable to take into account the post-peak behavior, i.e., strain-softening behavior in tension (and compression), particularly for the performance of crack initiation.

It is not the purpose of this paper to provide a robust design procedure for GRCS embankments. Instead, it is more of a fundamental work to answer how the strain-softening effect influences the progressive failure mechanisms of GRCS embankments. For such a purpose, an advanced constitutive model (referred to as the "Concrete" model hereafter) was introduced to model the DCM columns. The Concrete model was initially developed by Schädlich and Schweiger [29] to model the post-peak behavior of sprayed concrete lining (SCL) tunnels, and subsequently to model jet-grouting slab, and mixed-in-place columns in the context of deep excavations [7,39]. The Concrete model has been proven capable of realistically capturing the softening behavior of cement-based columns in compression and/or tension. The critical features of this model on the application in GRCS embankments over soft soils will be presented later.

In this study, the progressive failure mechanisms of the DCM columns under embankment loading are studied by means of the FEM incorporating the strain-softening effect. A representative numerical model of the GRCS embankment resting on soft soils is first established. The Concrete model parameters are empirically determined and calibrated by the results of published uniaxial compression tests and three-point bending tests. The FEM model is then established to validate against previous centrifuge testing results. Subsequently, new insights into the progressive failure mechanisms of a GRCS embankment are provided from the viewpoints of effective stress paths, internal force, crack, and plastic failure zone development of DCMs. The influence of compression and tension parameters of DCMs, as well as the tensile stiffness of geosynthetics on the internal forces and failure sequence, are also explored.

2. Numerical analysis

2.1. Problem definition

The widely-reported case history of a geosynthetic-reinforced DCM column-supported embankment constructed over a very soft soil deposit in Hertsby, Finland was chosen as the basis of this numerical study.[11,12,46] For simplification, only a representative embankment section was selected to construct a plain-strain numerical model, where the geometric configuration of the embankment was slightly adjusted. Such simplification allowed more columns to be included in the base model for fully interpreting the failure mechanisms and also allowed for the use of very fine mesh to capture the development of column cracks under embankment loading. For such reasons, it is not intended to provide a direct comparison against in situ measurements in this study.

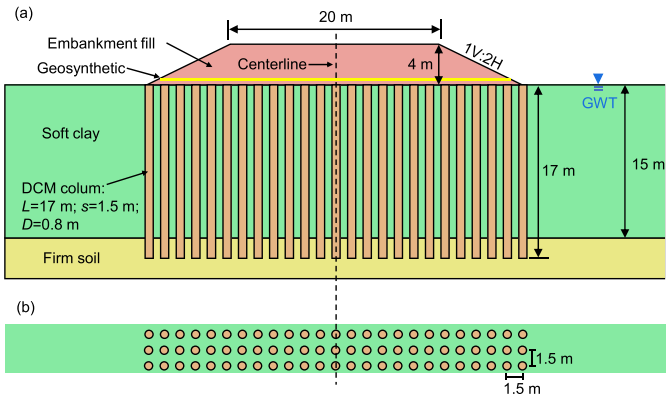

Fig. 1. GRCS embankment in the base case: (a) cross-sectional view and (b) plan view.

Table 1
Material parameters used in the MC model.

Parameter	Embankment fill	Soft clay	Firm soil
Drainage condition	Drained	Undrained (A)	Drained
Flow rule	Associated	Non-associated	Associated
Unit weight, γ (kN/m^3)	18	18	18
Elastic modulus, E (Mpa)	30	30	30
Poisson's ratio, ν (-)	0.3	0.3	0.3
Effective cohesion, c' (kPa)	5	0	0
Effective friction angle, φ' (°)	32	25	30
Dilatancy angle, ψ (°)	32	0	30

An embankment with a fill height of 4 m and a crest width of 10 m was constructed over a 15 m deep soft clay underlying a 5 m deep firm soil. The side slope gradient was 1: 2 (1*H*: 2 *V*). The groundwater table (GWT) is situated at the existing ground surface. Fig. 1 presents a cross-section of the GRCS embankment and a square arrangement of DCM columns (diameter of 0.8 m and spacing of 1.5 m). The isolated DCM column was embedded into the firm soil layer with a length of 2.0 m. For enhancing the embankment stability, a geosynthetic layer with tensile strength of 200 kN/m and tensile stiffness of 2500 kN/m was placed above 0.5 m column top to facilitate the uniform embankment load by the membrane effect. The material properties of foundation soils and embankment fill have been determined by the site investigation and further compiled from Huang and Han [11,12], as shown in Table 1. These parameters are not discussed in the following as the emphasis of this study is on the behaviors of columns and geosynthetics, particularly on the strain-softening behavior of columns.

2.2. Finite-element model set-up

All analyses were performed by the finite element code Plaxis 2D (Kumarswamy et al., 2016). A two-dimensional symmetrical plane-strain numerical model was set up based on the problem definition. Fig. 2 gives the finite-element (FE) mesh of a GRCS embankment. To balance computational cost and accuracy, a non-structured mesh was adopted to refine the columns and the geosynthetics. The soil domain was discretized with 15-noded triangular solid elements, and a total of around 13,000 elements were used. Other than rigid concrete piles, DMC columns, and surrounding soils have been proven to have good bonding, resulting in the shear strength of the interfaces between them may be

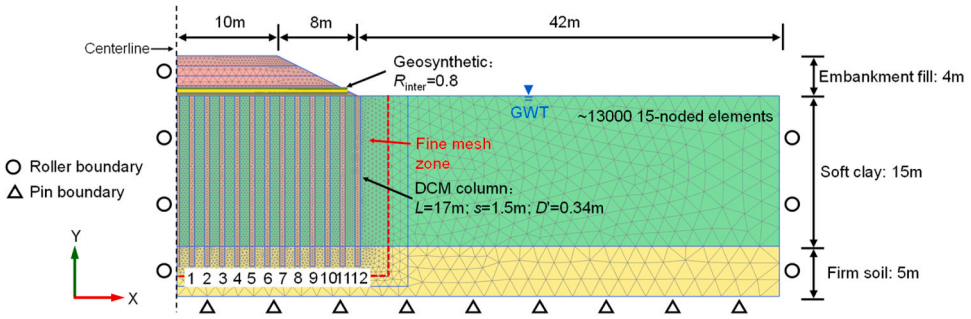

Fig. 2. Geometry, finite-element mesh, and boundary conditions.

higher than soil shear strength [27,49]. Therefore, no interface was set along the edge of the columns. The geosynthetic layer was simulated using 10-noded interface elements with 5 Gauss integration stress points to consider soil-structure interaction. To avoid the boundary effect, the soil domain was extended to 60 m. The horizontal displacements of the lateral boundary were constrained ($\Delta x = 0$), a full-fixity was prescribed at the bottom boundary ($\Delta x = 0$, $\Delta y = 0$), while the top boundary was free.

The linear elastic perfectly plastic Mohr-Coulomb failure criteria were adopted to simulate foundation soils and embankment fill as well as geosynthetics, of which the material parameters can be found in Table 1. During the elastoplastic calculations, the soft clay was set as undrained conditions in which the option of "Undrained A" in Plaxis 2D was chosen to calculate soil strength in terms of effective stress parameters [3]. The other materials (firm soil, embankment fill, and columns) were considered as drained conditions. To avoid the potential numerical instability due to the flow rule made, the non-associated and associated flow rules had to be used respectively to simulate soft clay (undrained) and other soils (drained), as highlighted by Tschuchnigg et al. [34], Schweiger and Tschuchnigg [30] and Lai et al. [20]. It means that a dilation angle of $\psi' = 0°$ was considered to model the soft clay while $\psi' = \varphi'$ was used to model the embankment fill and the base firm soil, as listed in Table 1. Moreover, the Concrete model was selected to simulate DMC columns for considering the strain-softening effect, which will be explained later in more detail.

It should be noted that the column-soil interaction is a three-dimensional problem in nature. To more realistically reflect the column-soil interaction, the equivalent area method originally presented by Bergado and Long [2] was employed to modify the diameter of the columns using the equation below:

$$D' = \pi D^2 / 4s \tag{1}$$

where D' is the equivalent column diameter, D is the diameter of isolated DCM columns and s is the center-to-center spacing of columns. The equivalent column diameter is 0.34 m in the present study (see Fig. 2).

The numerical analysis was then conducted following the usual procedure: (a) generation of the initial stress filed with the K_0-approach; (b) installation of the DCM columns using the wished-in-place method; (c) filling the embankments in layers per meter; and (d) loading on the embankment crest in steps per kPa until plastic failure.

Before running the 2D model, the effectiveness and feasibility of the equivalent area method under plain strain conditions have to be discussed. For such purpose, Appendix A provides thorough comparisons of constitutive responses in columns, stresses on geosynthetic reinforcement and column top as well as internal forces of columns, which are obtained from 2D/3D models, respectively. The comparisons proven the eddective use of the 2D model with an equivalent area method is a suitable choice, achieving a balance between computational efficiency and accuracy. The feasibility of the equivalent area method under plain strain conditions has been also demonstrated in the work by Yapage et al. [45,46] and Zhang et al. [50].

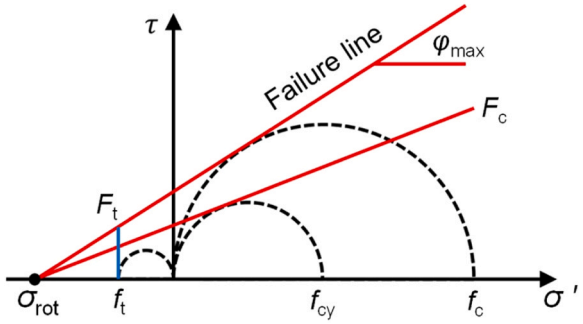

Fig. 3. Yield surfaces and failure envelope.

2.3. Constitutive model for DCM columns

Two constitutive models, i.e., the Mohr-Coulomb (MC) model with tension cut-off and the advanced Concrete model, were used to simulate DMC columns, respectively. The tensile strength of columns was input to cut off the tension in the MC model. The other parameters of the MC model were fully consistent with those reported by Huang and Han [11,12], hence they are omitted here. The Concrete model was newly developed by Schädlich and Schweiger [29] to simulate shotcrete linings in tunneling. The Concrete model comprehensively considers time-dependent strength and stiffness, strain-hardening and strain-softening as well as shrinkage. Since this paper primarily studies the evolution of internal force and failure as the cracks developed in the DCM columns after curing, the time-dependent features were switched off. Only a brief introduction of key features in the Concrete model relevant to the present study is provided here.

In the model, plastic strains are determined in light of strain hardening/softening elastoplasticity. MC yield surface (F_c) and the Rankine yield surface (F_t) is employed for deviatoric loading and tensile loading, respectively, as shown in Fig. 3.

The normalized stress-strain curve in compression is plotted in Fig. 4 (a). Strain hardening in compression (part I) first follows a quadratic function, with subsequent bi-linear softening (parts II and III) and a residue (part IV), as shown in Fig. 4(a). A normalized parameter of $H_c = \varepsilon_3^p / \varepsilon_{cp}^p$ is defined to bound hardening and softening in various stages, where ε_3^p is minor (compressive) principal plastic strain and ε_{cp}^p is plastic peak strain in uniaxial compression. Also, all compression strengths are normalized by peak strength i.e. $f_{cy} = \sigma_3 / f_c$. From Fig. 4(a), compression hardening with an initial strength (f_{c0n}) starts from $H_c = 0$, and then $H_c = 1.0$ indicates full mobilization of $f_{cy} = 1.0$. Then the linear softening to a normalized failure strength (f_{cfn}) occurs at $H_c = H_{cf}$, which is governed by the compression fracture energy of G_c. Full compression softening to a normalized residual strength (f_{cun}) is eventually reached at $H_c = H_{cu}$. Eqs. (2–5) characterize the compressive strength in the whole process of compression hardening/softening:

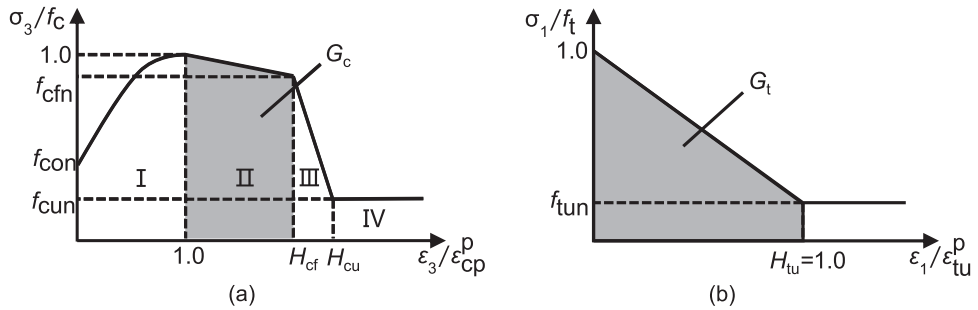

Fig. 4. Normalized stress-strain curves in: (a) compression and (b) tension.

Table 2
Model parameters of cement soils.

Description	Parameter	Unit	Base case		Uniaxial compression test			Three-point bending test			Centrifuge test	
			Concrete model	MC model	Concrete model		MC model	Concrete model		MC model	Concrete model	MC model
					Empirical	Calibrated		Empirical	Calibrated			
Unit weight	γ	kN/m^3	20	20	20	20	20	20	20	20	17	17
Young's modulus	E_{28}	MPa	30	30	289	424	424	540	2000	2000	200	200
Poisson's ratio	ν	-	0.30	0.30	0.30	0.30	0.30	0.17	0.17	0.17	0.45	0.45
Maximum friction angle	φ_{max}	°	30	30	30	30	30	30	30	30	0	0
Maximum dilatancy angle	ψ_{max}	°	0	0	0	0	0	0	0	0	0	0
Uniaxial compressive strength	$f_{c,28}$	kPa	311	NA	963	963	NA	1800	1800	NA	758	NA
Normalised initially mobilized strength	f_{con}	-	0.60	NA	0.60	0.78	NA	0.60	0.60	NA	0.60	NA
Normalised failure strength	f_{cfn}	-	0.75	NA	0.75	0.60	NA	0.75	0.70	NA	0.75	NA
Normalised residual strength	f_{cun}	-	0.20	NA	0.20	0.25	NA	0.20	0.20	NA	0.20	NA
Compressive fracture energy	$G_{c,28}$	kN/m	5.0	NA	5.0	6.5	NA	5.0	5.0	NA	5.0	NA
Uniaxial plastic failure strain	ε_{cp}^{p}	-	0.003	NA	0.003	0.002	NA	0.003	0.003	NA	0.003	NA
Uniaxial tensile strength	$f_{t,28}$	kPa	47	47	144	144	144	270	380	380	114	114
Ratio of residual to peak tensile strength	f_{tun}	-	0	NA	0	0	NA	0	0	NA	0	NA
Tensile fracture energy	$G_{t,28}$	kN/m	0.01	NA	0.01	0.01	NA	0.01	0.01	NA	0.01	NA
Effective cohesion	c'	kPa	NA	90	NA	NA	278	NA	NA	520	NA	219

Note: NA = Not applicable

$$f_{cy,I} = f_c\left[f_{con} + (1 - f_{con})\left(2H_c - H_c^2\right)\right] \quad (2)$$

$$f_{cy,II} = f_c\left[1 + \left(f_{cfn} - 1\right)\left(H_c - 1/H_{cf} - 1\right)\right] \quad (3)$$

$$f_{cy,III} = f_c\left[f_{cfn} + \left(f_{cun} - f_{cfn}\right)\left(H_c - H_{cf}/H_{cf} - H_{cu}\right)\right] \quad (4)$$

$$f_{cy,IV} = f_c{\cdot}f_{cun} \quad (5)$$

In Fig. 4(b), a linear softening in tension can be found until a residual tensile strength of f_{tun} is reached. Similar to the compression, a normalized tension-softening parameter ($H_t = \varepsilon_1^p/\varepsilon_{tu}^p$) and a normalized tensile strength ($f_{ty} = \sigma_1/f_t$) are both defined, where ε_1^p is major (tensile) principal plastic strain and ε_{tu}^p is plastic peak strain in uniaxial tension, σ_1 is tensile strength and f_t is a peak (initially) tensile strength. Therefore, the normalized post-peak tensile strength follows:

$$f_{ty} = f_t[1 + (f_{tun} - 1)H_t] \quad (5)$$

More detail of the Concrete model can be found in Schädlich and Schweiger [29]. Appendix B also presents how the initial model parameters relevant to the purpose of this study are determined empirically.

Table 2 further summarizes a set of empirical parameters used in the base model according to Appendix B and Table B1. As mentioned

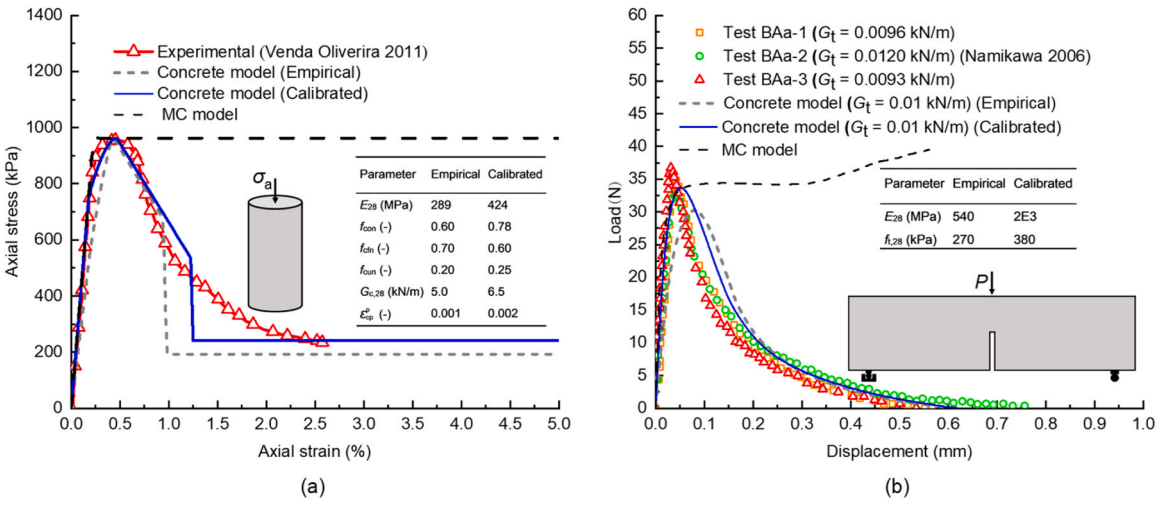

Fig. 5. Numerical comparison against: (a) uniaxial compression test and (b) three-point bending test.

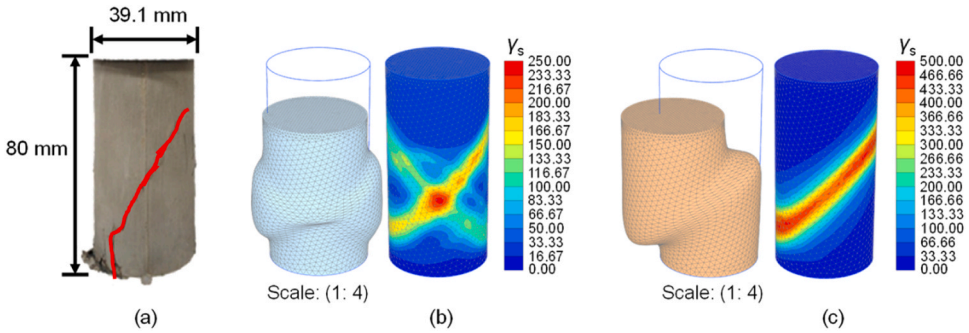

Fig. 6. Shear bands of specimens observed from: (a) uniaxial compression test; (b) MC model; and (c) Concrete model.

previously, the base model in this study was established based on a real project in spite that no available experimental data has been provided to calibrate the model parameters. Therefore only empirical but reasonable data (proven later) is presented here. For this reason, the $f_{c,28}$ was first converted from the MC model parameters reported by Huang and Han [11,12], and then the other parameters of the Concrete model were empirically estimated using the correlations listed in Table B1. All the strength and stiffness parameters of the cured DCM columns used here corresponded to standard values after 28 days since all the time-dependency features have been switched off.

2.4. Concrete model validation against laboratory results

To examine whether the Concrete model can accurately capture strain-hardening/softening behaviors in compression and/or tension, the previous test results are used to compare with those from the model. The uniaxial compression test by Venda Oliveira et al. [38] and the three-point bending test by Namikawa and Koseki [24] are numerically modeled on a realistic scale with the Concrete model and MC model, of which the empirical and calibrated model parameters are then tabulated in Table 2.

Figs. 5(a) and 5(b) present a comparison of the results obtained from the published uniaxial compression test and three-point bending test, respectively. It follows from Fig. 5(a) that the axial stress-strain curve

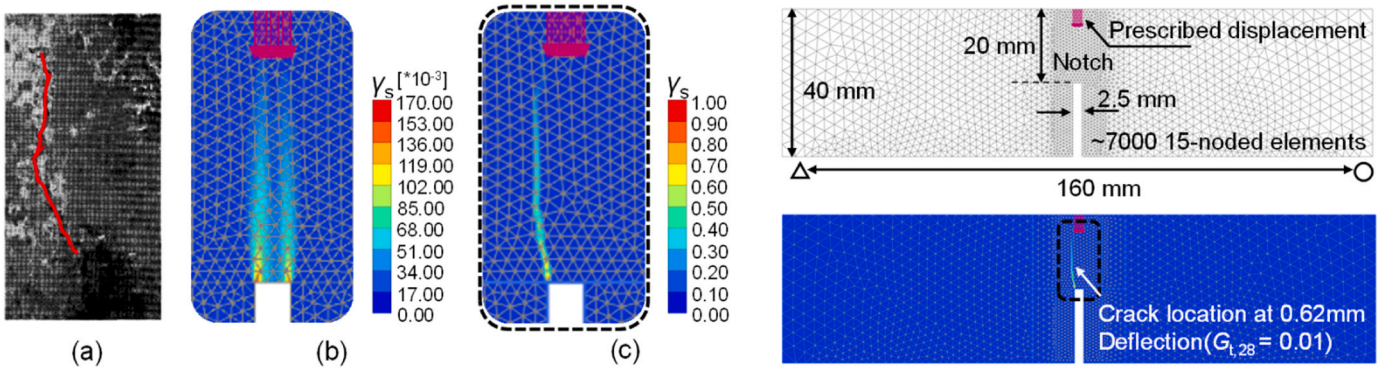

Fig. 7. Deviatoric shear strain of specimens from: (a) three-point bending test; (b) MC model and.

Table 3
Material parameters used in MC model for modeling centrifuge test.

Parameter	Embankment fill	Sand layer	Clay layer	Clay between DCM columns
Drainage condition	Drained	Drained	Undrained (B)	Undrained (B)
Flow rule	Associated	Associated	Non-associated	Non-associated
Unit weight, γ (kN/m^3)	21	21	17	17
Elastic modulus, E (Mpa)	150	300	30	3
Poisson's ratio, ν (-)	0.33	0.33	0.45	0.45
Effective cohesion, c' (kPa)	0	0	NA	NA
Effective friction angle, φ' (°)	35	35	NA	NA
Undrained strength, S_u (kPa)	NA	NA	120	12
Dilatancy angle, ψ (°)	35	35	0	0

Note: NA = Not applicable

Table 4
Comparison of the ultimate surcharge loadings of an embankment.

Parameters		Strength of DCM columns (kPa)	Area replacement ratio (%)	Ultimate surcharge (kPa)
Numerical simulate	MC model	758	79	986
	Concrete model			894
Centrifuge test				856

from the Concrete model after calibration presents a good agreement with experimental results. The comparison between the Concrete model and the MC model in Fig. 5(a) shows the change of compressive strength in various stages is well reproduced by the Concrete model, but only peak compressive strength is reflected in the MC model. Fig. 5(b) indicates that the load-displacement curve from the Concrete model matches perfectly with the experiment results, regardless of whether the model is calibrated. Although the small difference between numerical and experimental results is observed in Fig. 5(a) for the Concrete models with empirical parameters, compression-hardening/softening and tension-softening behaviors in specimens can also be captured.

To further demonstrate the advantages of the Concrete model for modeling cement-based soil, the shear bands (deviatoric strain and deformed mesh) of specimens obtained numerically and experimentally in the uniaxial compression test and three-point bending test are compared in Fig. 6 and Fig. 7, respectively. The calibrated model parameters are adopted here. It can be seen from Fig. 6 that a barrel-shaped specimen with un-concentrated deviatoric strain is obtained in the MC model, whereas a clear strain localization, in line with experimental observations, is presented in the Concrete model. Again, perfect agreement of cracks between the numerical and the experiment results is observed in Fig. 7. It was therefore concluded that the Concrete model is capable of correctly capturing the strain-hardening/softening behavior and reasonably reflecting the cracks developed in cement-based soil.

2.5. FE model validation against centrifuge tests

The FE model is further validated against centrifuge tests in Kitazume et al. [15], in terms of ultimate surcharge load and plastic failure zone. Note that both the MC model and the Concrete model are presented in the study. Table 3 presents the MC model parameters, drainage conditions, and flow rules used for the validation, whilst the material parameters of the DCM columns are given in Table 2.

Table 4 compares the ultimate surcharge loading of the embankment supported with the DCM columns (with strength of 758 kPa and 79% area replacement ratio) modeled using the MC model and the Concrete model. Results have shown that the use of the Concrete model attains a very close ultimate surcharge load with measured value (centrifuge test), with an error of 5%. However, the use of the MC model leads to an around 15% higher surcharge than the measured value. It can therefore be concluded that stability assessment of embankments using the MC model may result in unconservative results.

A comparison of the plastic failure zone obtained from the centrifuge test, MC model, and Concrete model is presented in Fig. 8. It follows that the use of the Concrete model yields a more localized (concentrated) plastic failure zone and hence a clearer shearing band, which is in line with the failure mechanisms reported by Kitazume et al. [15]. On the contrary, the introduction of MC model causes a very spread failure zone and hence an unclear fail mechanism. The comparison made here also explains why using the MC model leads to an unconservative result. In all, the proposed FE analyses with the Concrete model are considered accurate and reasonable, and they can be used to interpret progressive mechanisms and examine the role of columns and geosynthetics with great confidence.

3. Progressive failure mechanisms

3.1. Stress paths

To understand the progressive failure mechanisms of GRCS embankments, stress paths of two representative points (i.e. points A and B)

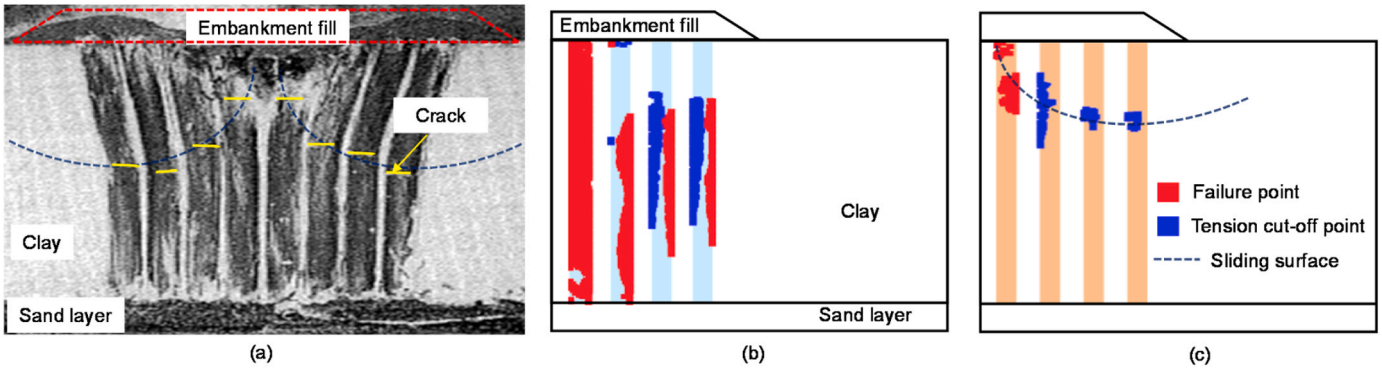

Fig. 8. Development of plastic failure zone: (a) Centrifuge test (form [15]); (b) MC model; (c) Concrete model.

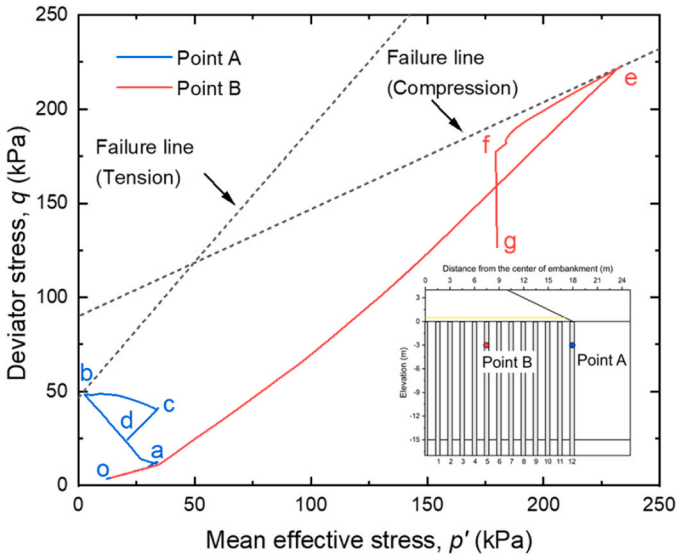

Fig. 9. Effective stress paths of Points A and B.

in columns 12 and 5 at around 3 m depth below the surface, are plotted in Fig. 9. Here, columns 12 and 5 correspond to those located below embankment crest and side slope, respectively. Point A is mainly subject to bending moment and point B experiences both bending moment and vertical force. Significant cracks can be observed in columns 12 and 5 at a depth ranging from 2 m to 4 m below the surface (see Figs. 10 and 11). Hence, points A and B with a depth of 3 m are chosen as the typical points. The stress path changes in four typical stages can be observed for point A when increasing the embankment surcharge load: (1) compression hardening (path o-a); (2) rotation of principal stress axes, showing the stress state changes from compression to tension (path a-b); (3) tension softening, in which the stress state reaches the tension failure envelop with subsequent tension softening (path b-c) and correspondingly a stress relief; and (4) a tension cut-off (path c-d).

Three typical stages of the stress path change for point B are presented as the embankment surcharge load increases: (1) compression hardening (path o-e); (2) compression softening (path e-f) once the stress state reaches the compression failure line; and (3) compression failure (path f-g). These stress paths in Fig. 9 clearly show how the failure progresses in a GRCS embankment. Besides, the Concrete model is proven again to have the ability to correctly capture the strain hardening/softening behavior in compression/tension.

3.2. *Internal forces and cracks*

The development of internal forces (bending moment and internal force) and cracks of representative columns 5 and 12 as the embankment surcharge load q increases are presented in Figs. 10(a-b) and 11(a-b). The bending moment following counter-clockwise is postulated to be positive, while the tensile axial force is considered positive. It follows from Fig. 10(a) that once the q value increases to a certain value e.g. q = 14kPa, the cracks initiate in column 12 that is mainly subjected to

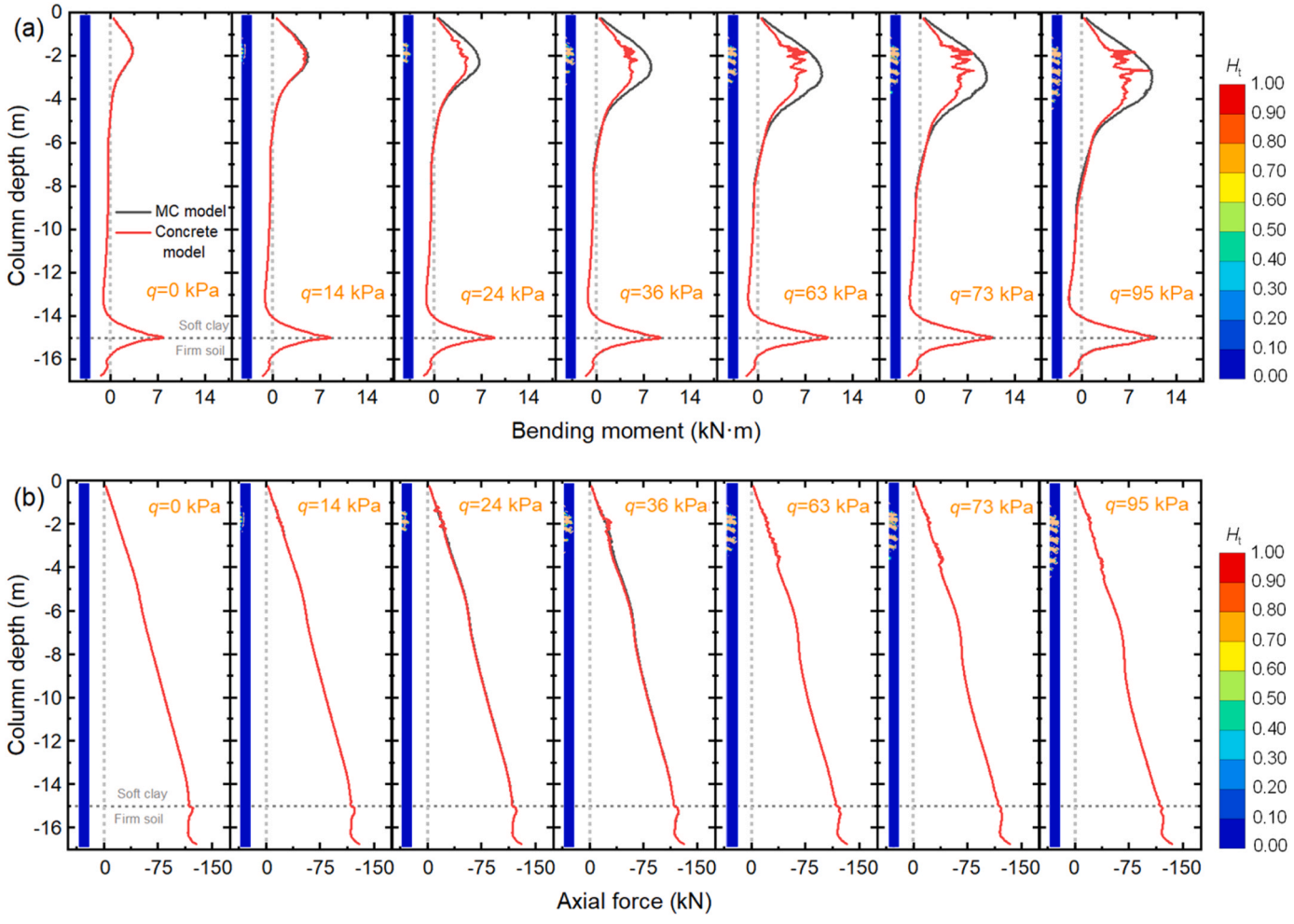

Fig. 10. Evolution of the internal forces and cracks of column 12: (a) bending moment; (b) axial force.

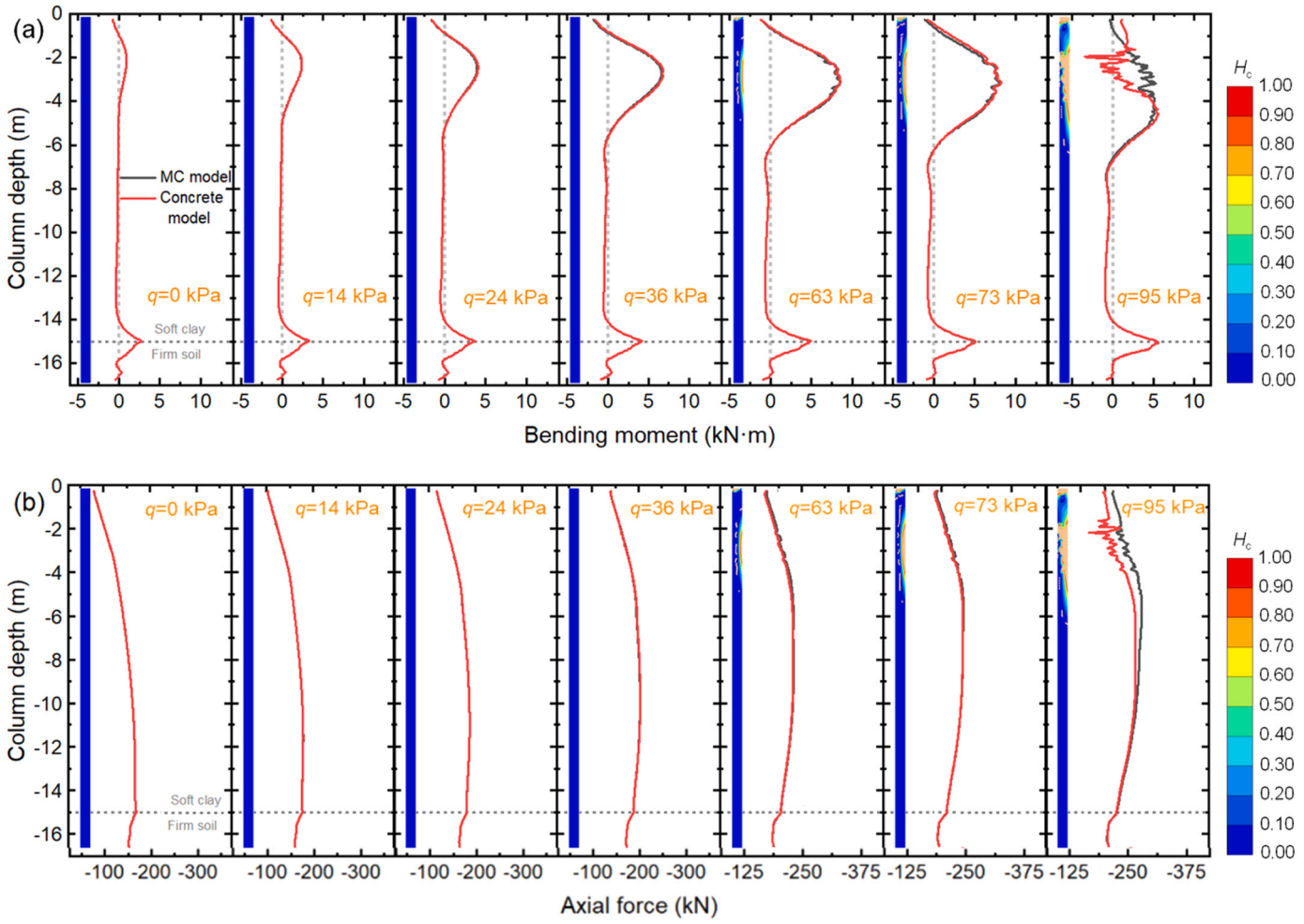

Fig. 11. Evolution of internal forces and cracks of column 5: (a) bending moment and (b) axial force.

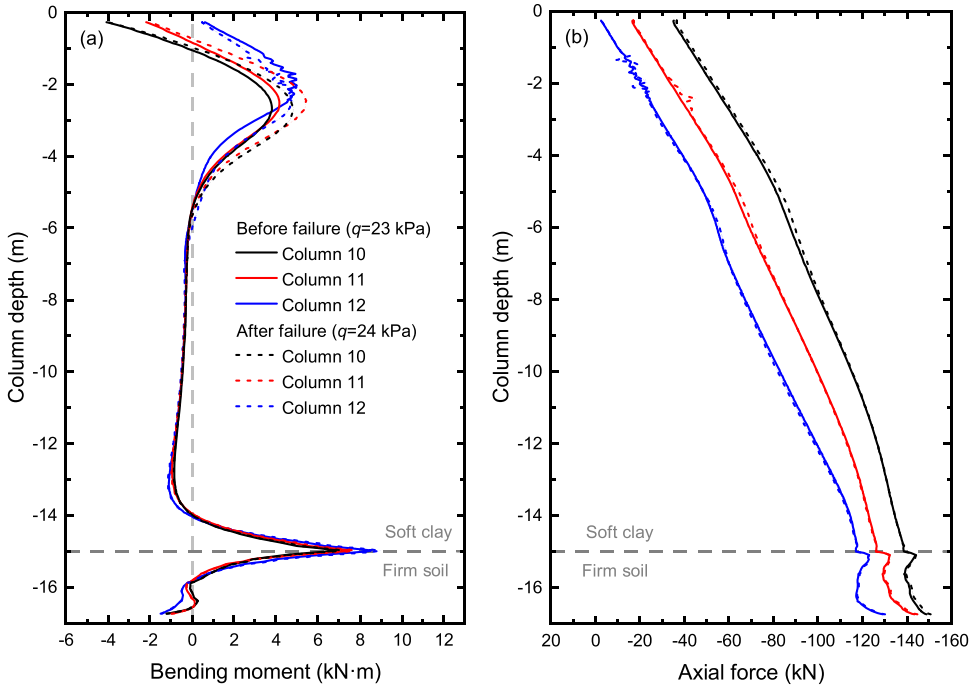

Fig. 12. Distribution of internal forces in columns 10 to 12 before and after failure: (a) bending moment and (b) axial force.

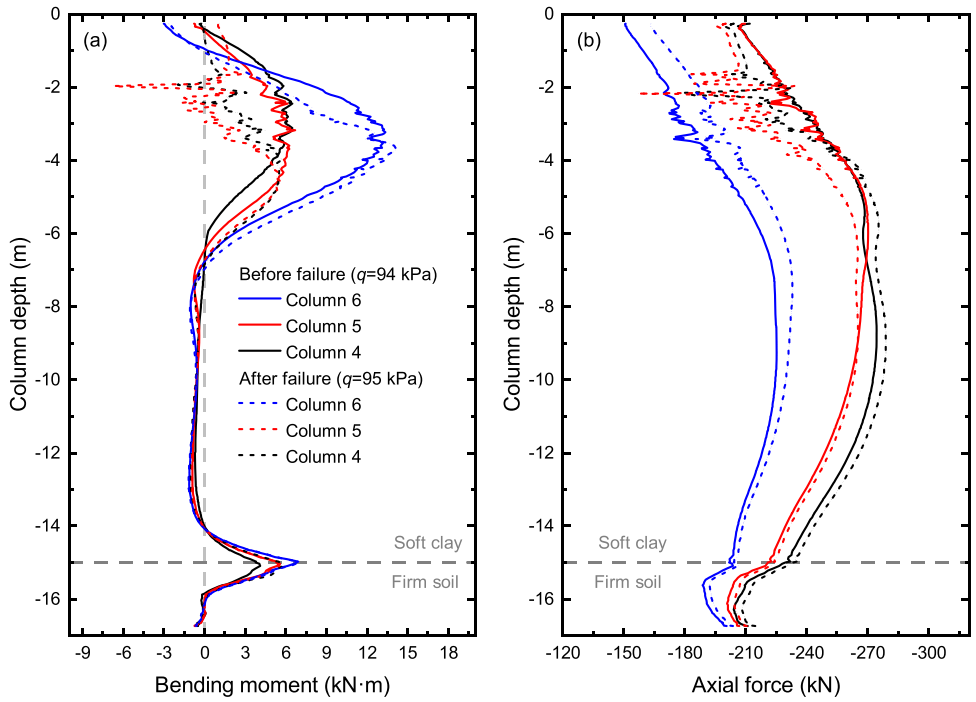

Fig. 13. Distribution of internal forces in columns 4–6 before and after failure: (a) bending moment and (b) axial force.

bending-induced tensile stress. As expected, the bending moment increases with increasing q value. The obvious changes in the bending moment of column 12 are found in depths 2 m ~ 4 m below the surface. In this zone, a reduction of bending moment as a consequence of tension-softening can be seen when compared with the results from the MC model. Furthermore, apparent oscillations in the curves of bending moment vs. depth are observed for the Concrete model as the tension-dominated cracks are developed in the columns, which is, of course, not considered in the MC model. Fig. 10(b) shows that the axial forces are unchanged as column 12 is mainly subjected to bending moment caused by the lateral thrusts.

Fig. 11 shows that for column 5, the compression-induced bending moment and axial force both increase with an increase in surcharge load. Before reaching the peak compressive strength (q $\leq$ 36 kPa), the approximately consistent responses of vertical loading to bending moment and axial force are found in both MC and Concrete models. After that, a gap between the two models is gradually widening as the compression-dominated cracks develop and then reach the maximum when the compressive strength softens to a residual value. These comparisons made in Fig. 10 and Fig. 11 highlight a significant role in considering the strain-softening behavior for the interpretation of progressive mechanisms of GRCS embankments.

To study the responses of the specific column failure (columns 5 and 12) to the surrounding columns, the changes in internal forces of two couples of columns (columns 4–6 and 10–12) before and after failure load are extracted from numerical results, as shown in Figs. 12 and 13. As mentioned earlier, the surcharge load increases stepwise per 1kPa until plastic failure occurs. Therefore, the responses before failure correspond to a case under the failure (ultimate) load minus 1kPa. It can be found from Fig. 12 that the failure of column 12 at 24 kPa leads to a loss of bending moment for itself but an increase for surrounding columns 10 and 11. However, the axial force remains unchanged, indicating that the column after tension-dominated (bending) failure still can carry the vertical load.

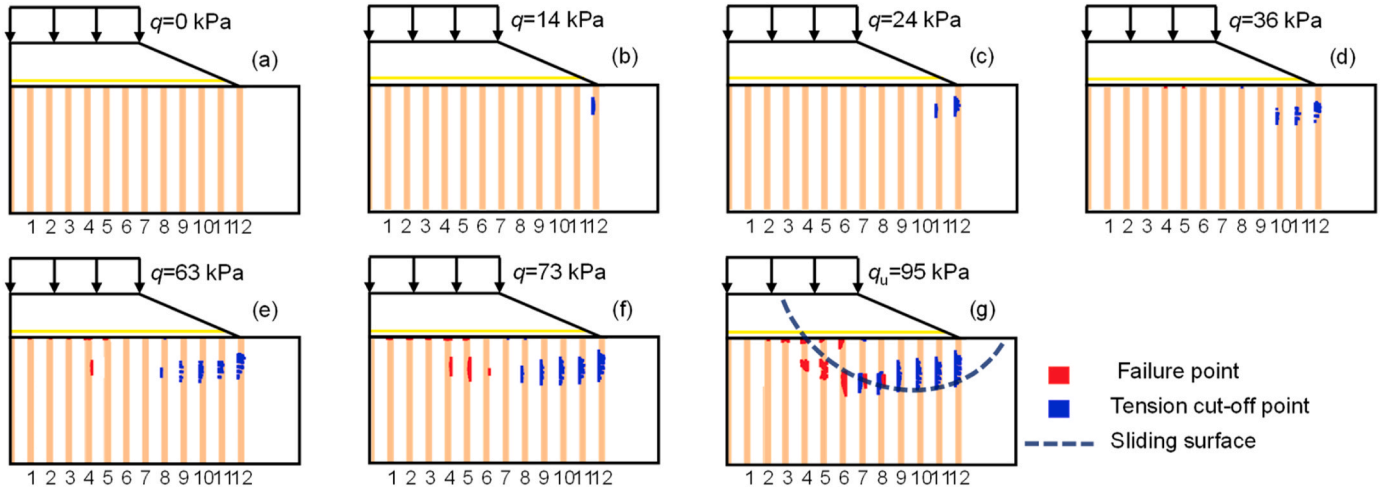

Fig. 14. Development of plastic failure zone: (a) q= 0 kPa; (b) q= 14 kPa; (c) q= 24 kPa; (d) q= 36 kPa (e) q= 63 kPa; (f) q= 73 kPa and (g) q= 95 kPa..

Table 5
Parameters for analysis of the role of columns and geosynthetics.

Set	Case	Columns				Geosynthetic	Remarks
		f_t (kPa)	G_t (kN/m)	f_c (kPa)	G_c (kN/m)	E (kN/m)	
A	Low f_t & Low G_t *	47	0.01	311	5.0	2500	Column 12
	Low f_t & High G_t	47	0.10				
	High f_t & Low G_t	150	0.01				
	MC model#	47	-	-	-		
B	Low f_c & Low G_c*	47	0.01	311	5.0	2500	Column 5
	Low f_c & High G_c		0.01	311	50.0		
	High f_c & Low G_c		0.01	1000	5.0		
	MC model#		-	-	-		
C	Weak reinforcement	47	0.01	311	5.0	1000	Columns 5
	Medium reinforcement*					2500	& 12
	Strong reinforcement					5000	
	Very strong reinforcement					10000	

Note: * = Base case
= Input parameters are described in Table 2

Fig. 13 shows that the compression-dominated (shear) failure of column 5 at 95 kPa leads to a pronounced reduction in both bending moment and axial force for columns 4 and 5, and a slight increase for column 6. This means that the compression failure of columns significantly causes stress losses which may be transferred to the surrounding columns. The comparisons between Figs. 12 and 13 signify that a column due to compression-induced shear failure can bear much higher internal forces than that tension-dominated bending failure to carry more vertical loads as the compressive strength is greatly larger than tensile strength. This inspires geo-engineers should have special attention to keeping the stability of the columns below the side slope for a GRCS embankment in soft soils.

3.3. Plastic failure zones

Fig. 14 plots the development of plastic failure zones in GRCS embankments as the failure progresses. It has shown that, as the surcharge load increases, the side columns 9 ~ 12 approach failures in tension due to bending. When increasing the surcharge load to a higher value e.g., q = 63 kPa, the compression-induced shear failure is first observed in column 4, followed by columns 5 and 6. The two sides of columns 7 and 8 are subjected to tension and compression failures, respectively. These results clearly show that the GRCS embankment has a progressive failure process until a sliding surface is formed. More discussion on failure sequence in progressive failure mechanisms will be given later by examining the role of columns and geosynthetics.

4. Role of the columns and geosynthetics

This section presents a sensitivity analysis of how tensile and compressive parameters of columns and tensile stiffness of geosynthetics influence the internal forces under different levels of surcharge loads. Table 5 summarizes three sets of parameters used for the sensitivity analysis. The analysis for set A takes into account different combinations of tensile parameters of column 12, i.e., peak tensile strength f_t and tensile fracture energy G_t. The analysis for set B considers different combinations of compressive parameters of column 5, i.e., peak compressive strength f_c and compressive fracture energy G_c. The comparison of results between the Concrete model and the MC model is also presented in sets A and B. The analysis for set C focuses on the variation

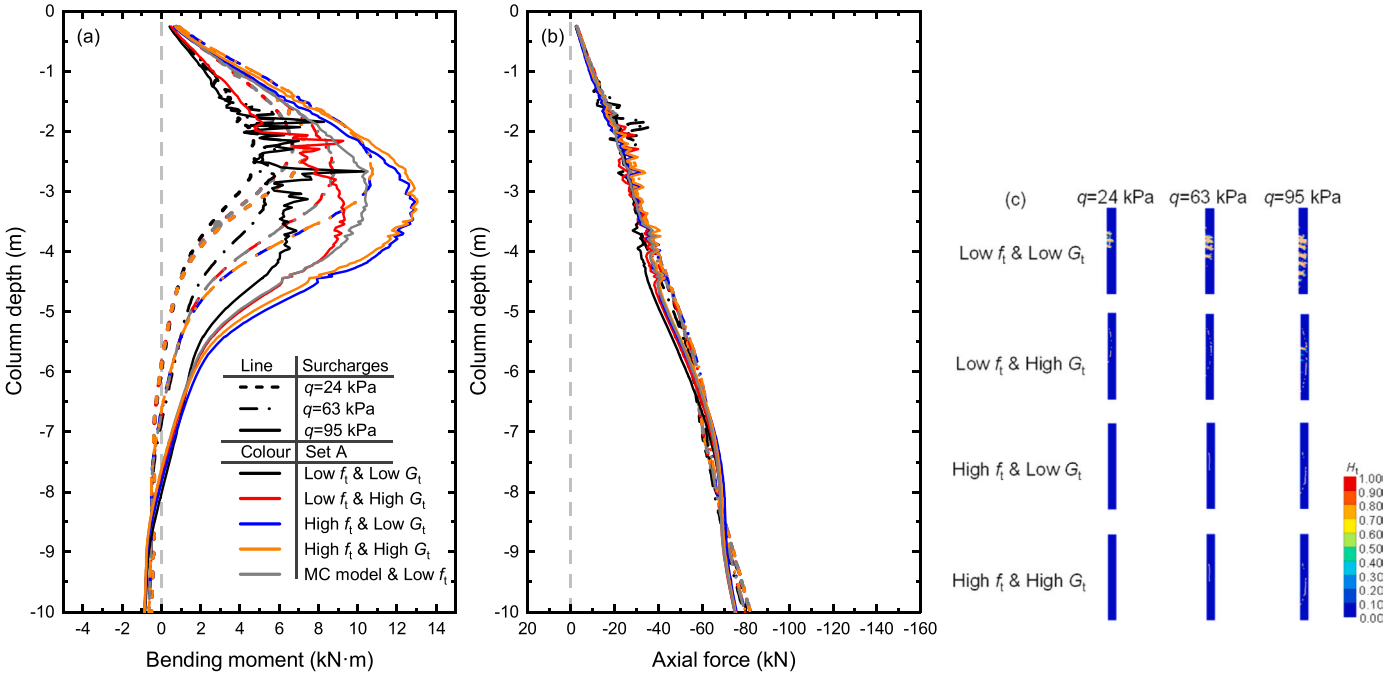

Fig. 15. Influence of tensile parameters on column 12: (a) bending moment; (b) axial force and (c) tensile cracks..

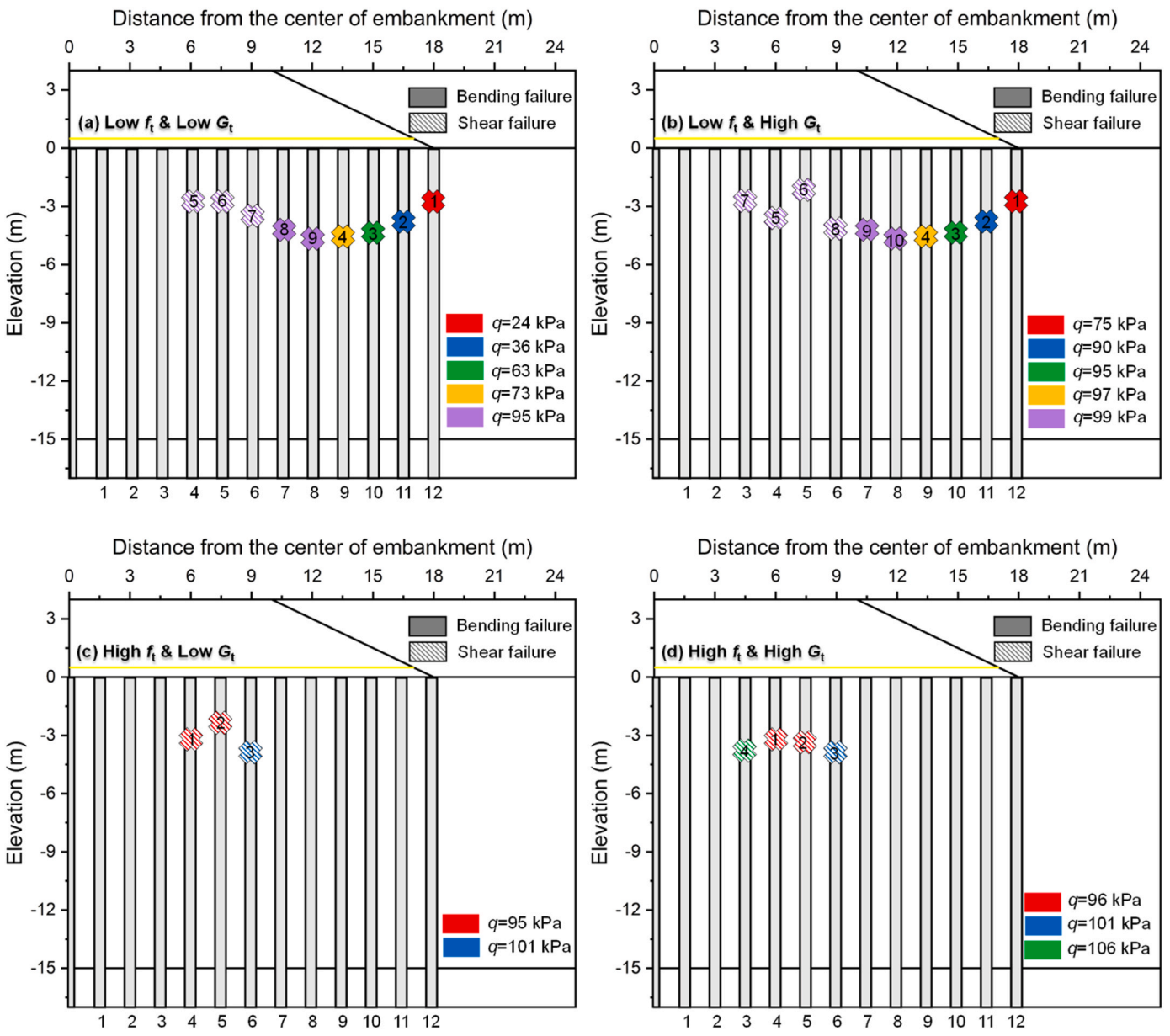

Fig. 16. Influence of tensile parameters on the column failure loads and sequences of GRCS embankments: (a) Low f_t & Low G_t; (b) Low f_t & High G_t; (c) High f_t & Low G_t and (d) High f_t & High G_t.

of tensile stiffness of geosynthetics (weak, medium, strong, and very strong reinforcement) of columns 5 and 12.

4.1. Tensile parameters of columns

Fig. 15 presents the development of internal forces and cracks of column 12 as embankment surcharge load q increases under different tensile parameter combinations (set A in Table 5). As is defined, higher f_t and G_t, respectively, mean that the higher surcharge load and the larger ultimate plastic strain are required to reach tensile failure. It follows from Fig. 15 that for the Low f_t & Low G_t, when the q value increases to 24 kPa, the tension-induced crack and failure occur in column 12 (see Fig. 15c); after that, the bending moment in the failure zone remains unchanged, but continue to increase in an un-failed zone. For Low f_t & High G_t, although the tensile failure has been observed in Fig. 15(c) even under $q = 63$kPa, the responses obtained from the Concrete model and MC model are very close. This is attributed to that a higher G_t leads to a lower (slower) tensile strain-softening rate. Once the q value increases to 95 kPa, the tensile plastic strain further increases and the tensile strength softens to a lower value, resulting in a noticeable difference in bending moment obtained between the two models, as shown in Fig. 15 (a).

For High f_t & Low G_t and High f_t & High G_t, since the tensile strength is high enough, even under $q = 95$ kPa, the cracks and failure do not happen in the column. As a result, the bending moment always increases with increasing the surcharge in the two cases above, and their bending moments under a fixed q are very close. Besides, the tensile parameters have a negligible effect on the axial force, which has been discussed and demonstrated before. It should be noted that the numerical oscillations of results are seen in failure zones, it is, however, argued that this does not influence the change laws as the vertical loads are still carried.

Fig. 16 shows the column failure loads and sequences of GRCS embankments as the q value increases for set A in Table 5. The progressive failure mechanisms formed in GRCS embankments are highlighted: the side columns first undergo bending failure with a subsequent shear failure for the central columns. Different combinations of tensile

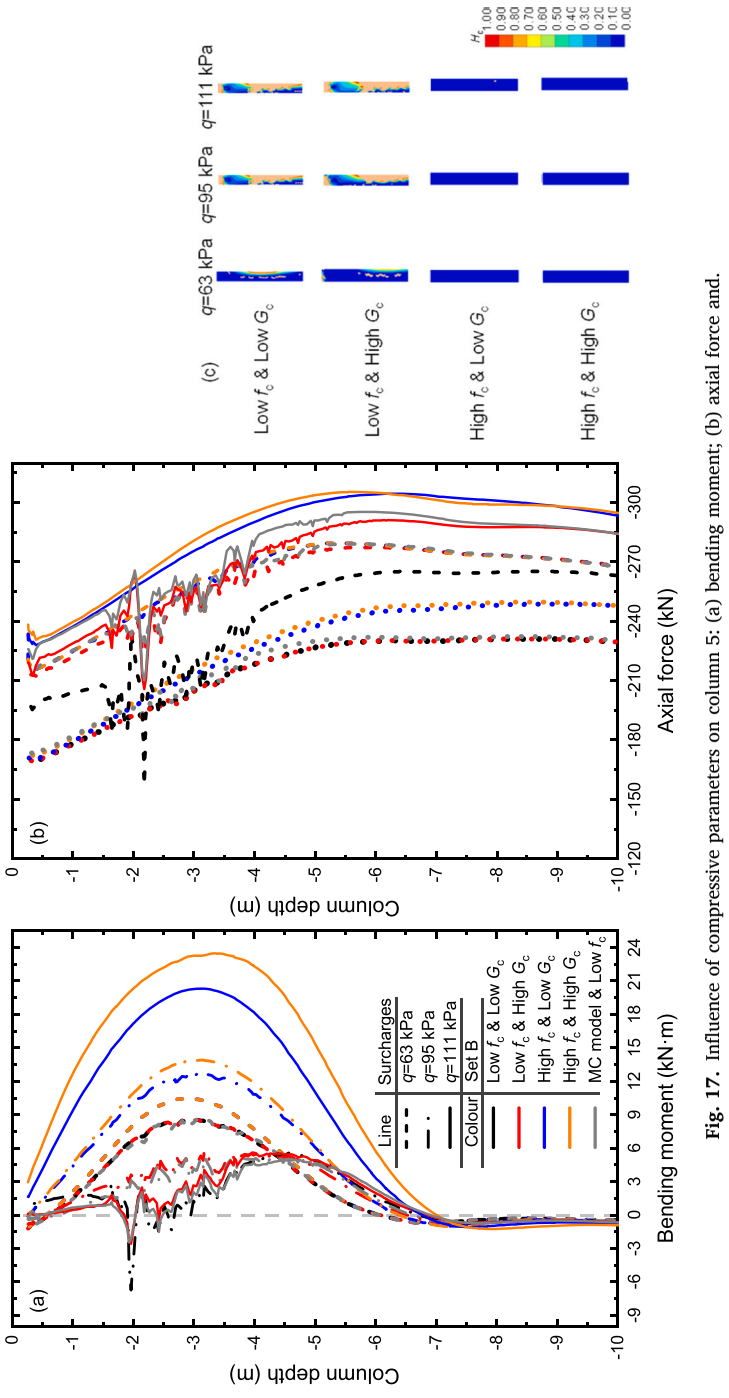

Fig. 17. Influence of compressive parameters on column 5: (a) bending moment; (b) axial force and.

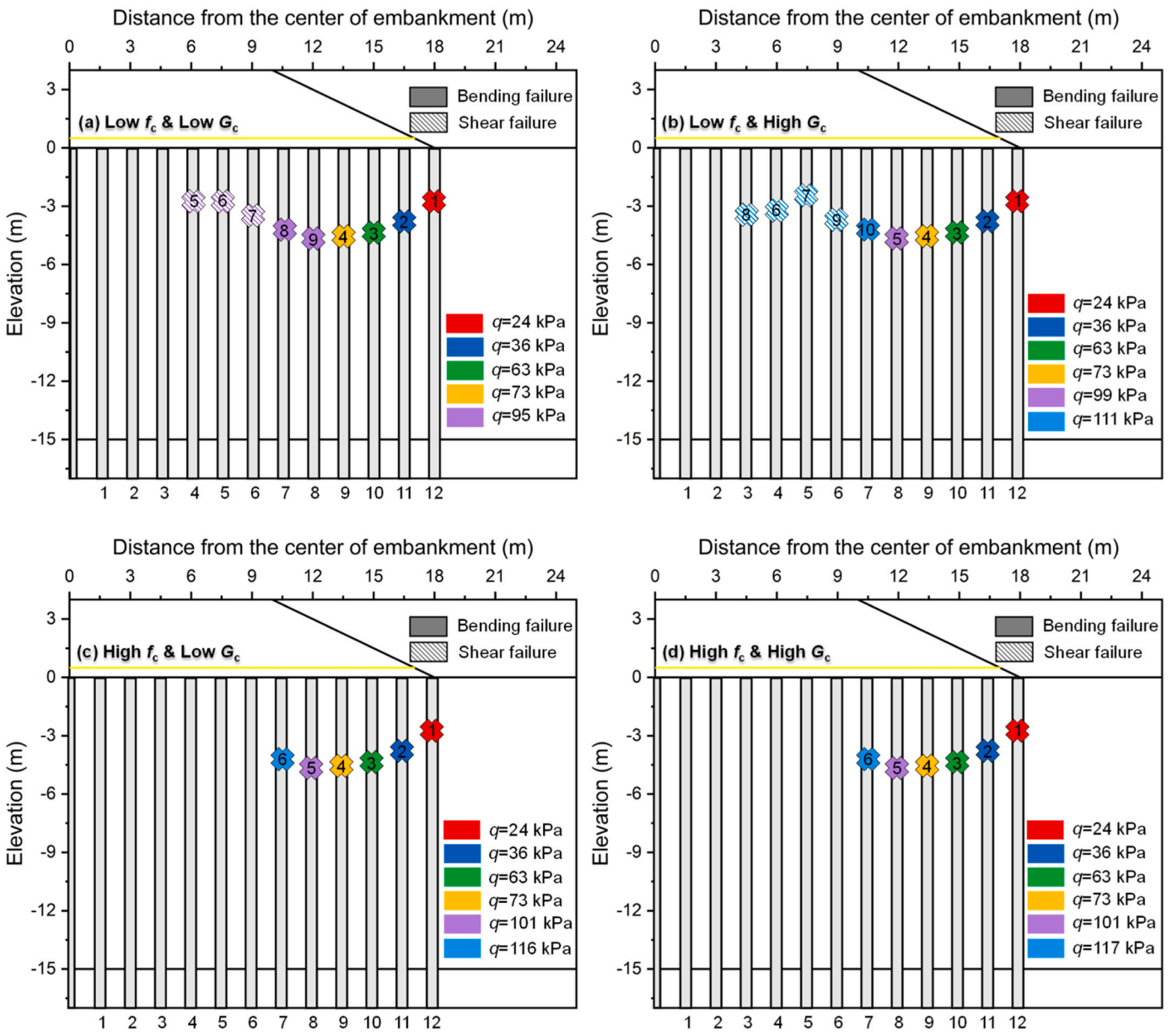

Fig. 18. Influence of compressive parameters on the column failure loads and sequences of GRCS embankments: (a) Low f_c & High G_c; (b) Low f_c & High G_c; (c) High f_c & Low G_c and (d) High f_c & High G_c.

parameters of columns have a significant influence on the progressive failure mechanisms. A higher G_t delays the failure of columns below the side slope. A higher f_t enhances the ability to resist the lateral thrust due to the surcharge imposed for side columns but forms a punching failure mode for the columns below the embankment crest. It can be concluded that, for an embankment supported reinforced-columns, more attention should be paid to central columns (compression zone) to avoid a more brittle failure.

4.2. Compressive parameters of columns

Fig. 17 plots the development of internal forces and cracks in column 5 as the embankment surcharge load q increases under different compressive parameter combinations (set B in Table 5). For the case of Low f_c & Low G_c, when increasing q from 63 kPa to 95 kPa, the compression-dominated cracks and failure are formed in column 5 (see Fig. 17c), resulting in reductions of bending moment and axial force are both apparently seen in Fig. 17(a). In the case of Low f_c & High G_c, since the ultimate plastic strain required increases, strength softening in compression caused by a surcharge of q = 95 kPa is very limited even if many cracks have been developed in columns (see Fig. 17c). The similar responses from Concrete model and MC model for Low f_c & High G_c with q= 95 kPa are consequently very close. However, if increasing q to be high enough such as 111 kPa, the compressive strength of column 5 gradually softens to a residual value, again causing a significant reduction in the internal forces. Although the cracks and failure are not found in column 5 for the cases of High f_c & Low G_c and High f_c & Low G_c when q increases from 95 kPa to 111 kPa, a significant increase in internal forces is surprisingly seen. The reasons will be explained in the next section.

(c) compressive crack.

Fig. 18 shows the column failure loads and sequences of GRCS embankments in set B listed in Table 5 as the q value increases. The compressive parameters have a noticeable influence on the progressive failure mechanisms: higher G_c delays the failure of columns below the embankment crest, and higher f_c enhances the ability to resist the

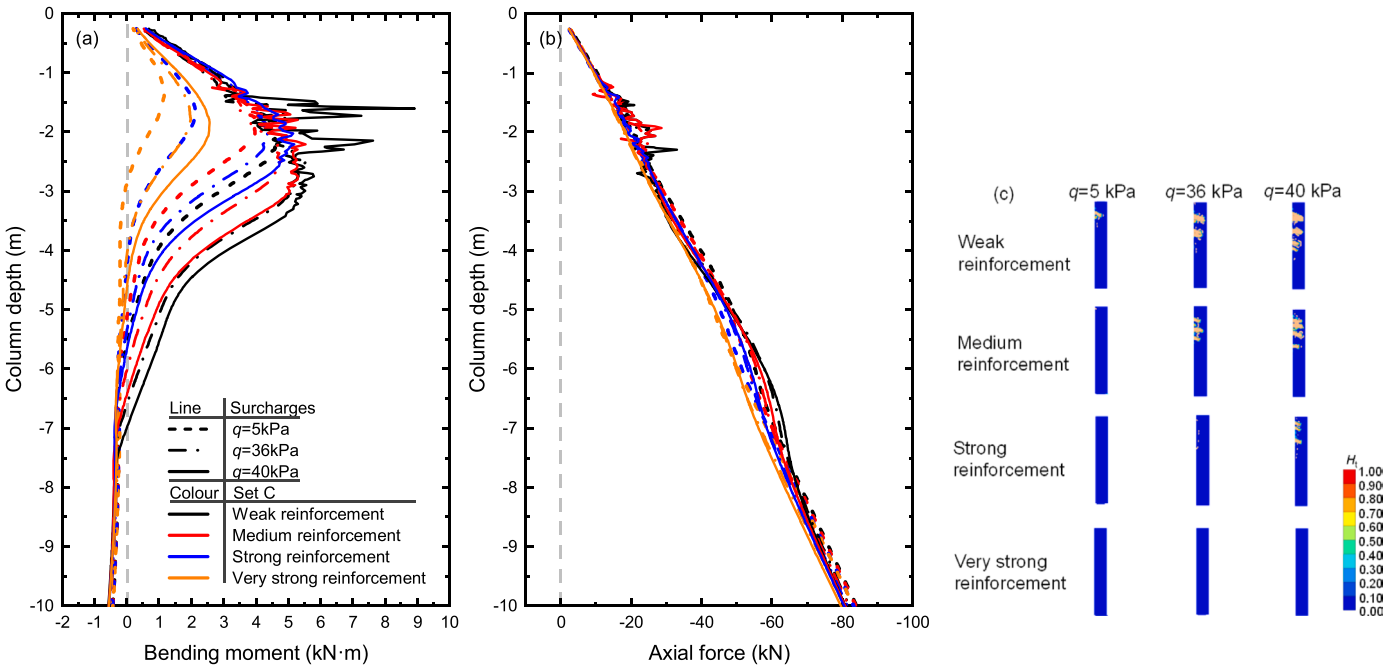

Fig. 19. Influence of tensile stiffness of geosynthetics on column 12: (a) bending moment; (b) axial force and (c) tensile crack.

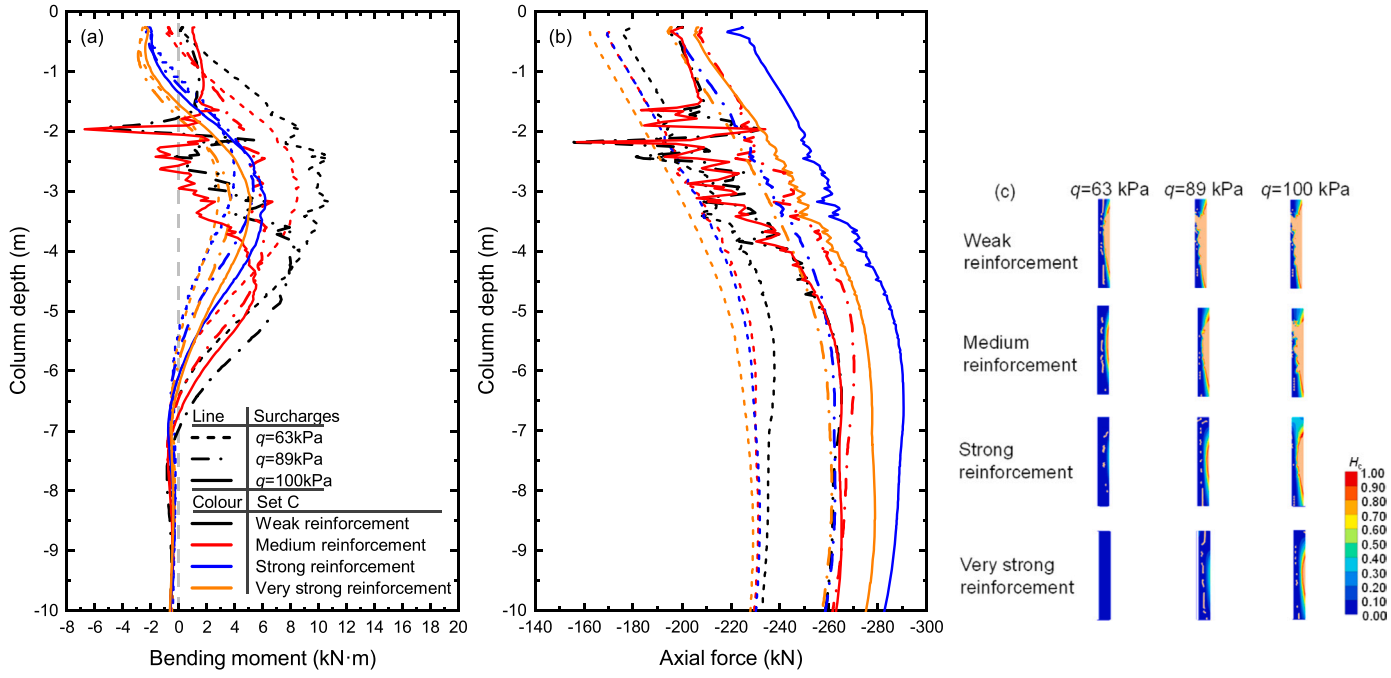

Fig. 20. Influence of tensile stiffness of geosynthetics on column 5: (a) bending moment; (b) axial force and (c) compressive crack.

embankment surcharge load. The general failure sequence (from side columns to central columns) for the case of Low f_c & Low G_c and Low f_c & High G_c can be observed, although the required ultimate surcharge loads for different columns in the two cases are highly different. For the cases of High fc & Low G_c and High f_c & Low G_c, only bending failure occurs in columns 7–12 of the GRCS embankment, indicating that the columns below the embankment crest are in a stable condition.

As shown in Figs. 18(c) and 18(d), as q increases from 95 kPa to 111 kPa, most of the surcharge load is carried by the central columns that are always in the elastic range, which is also subjected to significant stress relief from side columns. This explains why an unexpected increase in bending moment in column 5 is found. However, this treatment (using High f_c) seems to be unnecessary because a relatively lower value of f_c enables more columns and soils to be involved to obtain consistent bearing capacity. Therefore, a reasonable combination of compressive parameters is of significance to reduce the construction cost.

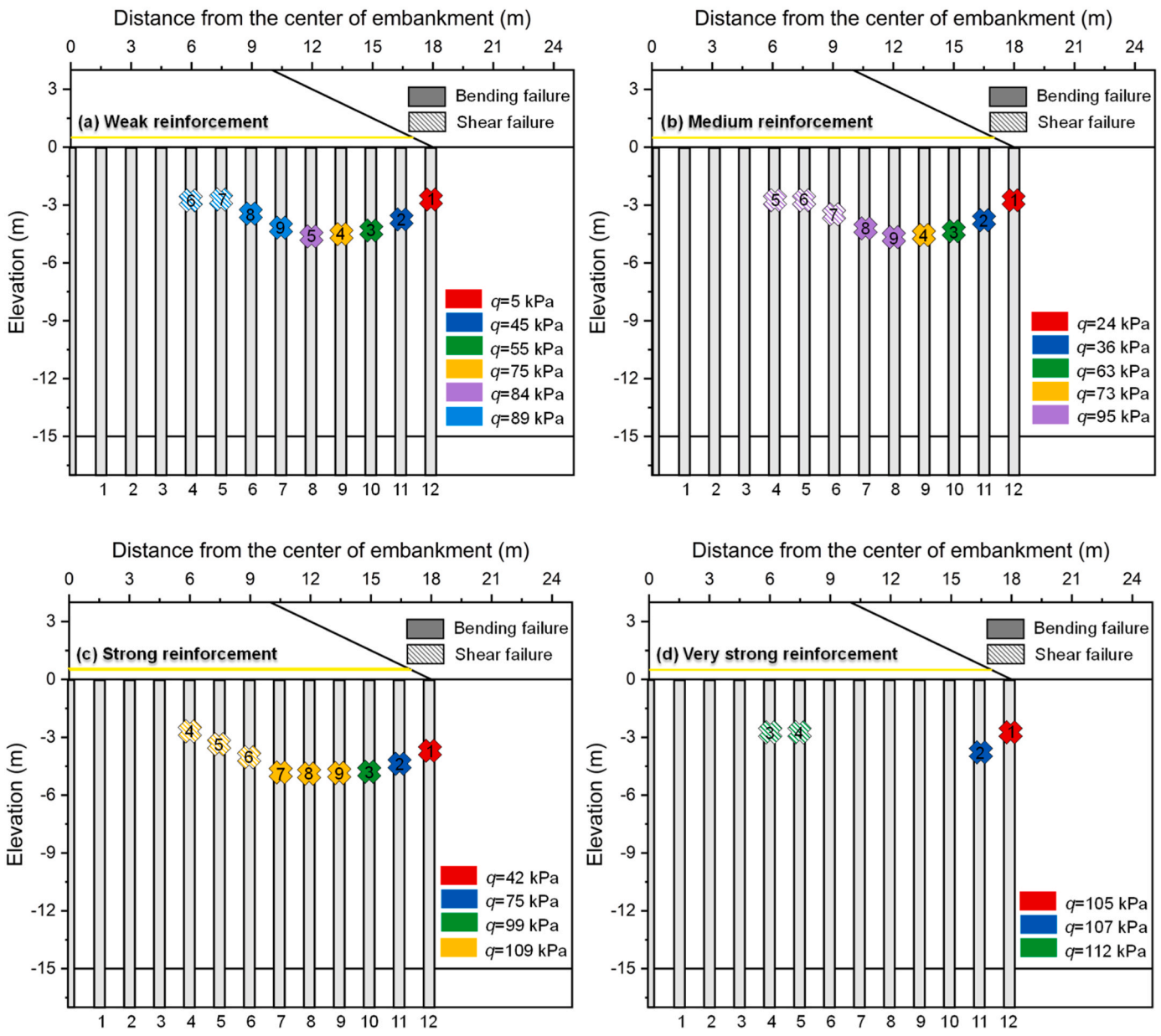

Fig. 21. Influence of tensile stiffness on the column failure loads and sequences of GRCS embankments: (a) weak reinforcement; (b) medium reinforcement; (c) strong reinforcement and (d) very strong reinforcement.

4.3. Tensile stiffness of geosynthetics

Figs. 19 and 20 presents the developments of internal forces and cracks of columns 12 and 5 respectively under different tensile stiffness E of geosynthetics as surcharge load q increases. It is well known that the introduction of geosynthetics would enable better distribution of the vertical loads on the soils under the membrane effect and the arching effect. This phenomenon is very noticeable for a higher tensile stiffness of geosynthetics. Therefore, the lateral thrust exerted by soils on side columns decreases with increasing E value, leading to a decrease in bending moment for elastic columns, as shown in Fig. 19(a). No crack is formed in column 12 when very strong reinforcement ($E = 10{,}000$ kN/m) is used under the loading levels studied (see Fig. 19c), but very clear cracks are seen for weak reinforcement ($E = 1000$ kN/m) and hence significant oscillations appeared in the curve of bending moment vs. depth. These results mean that increasing the tensile stiffness of geosynthetics strengthens the bearing capacity of the GRCS embankment.

In Fig. 20, column 5 has a less obvious increase in bending moment, but a very significant increase in axial force as the q value increases in the elastic zone. This is because the majority of embankment load is indeed transferred by the soil arching effect to columns. It is apparent in Fig. 20 that significant reductions in bending moment and internal forces due to cracks-induced softening behavior are introduced. However, the influence of changing tensile stiffness of geosynthetics on internal forces for columns below the embankment crest is hard to be quantified. The reason is that the vertical load on the columns may be increased or decreased under a combination of membrane effect and arching effect, particularly for strong or very strong reinforcement. It is

relevant to the load transfer mechanisms and beyond the scope of the present study. However, it can be justified that higher tensile stiffness of geosynthetics makes more bearing capacity of columns mobilized as the embankment load on the soil has been mostly transferred, which is particularly important for an embankment over soft soils.

The column failure loads and sequences for set C in Table 5 are further summarized in Fig. 21. When weak and medium reinforcements are used at the base of embankments, the general progressive failure sequence from side columns to central columns is shown (see Figs. 21a and 21b). For the case of strong reinforcement, more columns are in shear failure rather than bending failure (see Fig. 21c), indicating that higher tensile stiffness makes the vertical load transferrable onto columns due to the soil arching effect and hence being subjected to higher compressive stress. This is beneficial to enhance the bearing capacity of the GRCS embankment. On the other hand, for example, if very strong reinforcement is used ($E = 10{,}000$ kN/m), although the failure load in the bending failure zone increases significantly, the increase of bearing capacity of GRCS embankment is limited, as only punching failure is formed in shear failure zone. This is shown in Fig. 21(d). Therefore, it is desirable to conduct future research on evenly distributing embankment load on columns using reinforcement. This ensures that more columns could be in shear failure, which is desirable in design.

5. Conclusions

This paper has successfully studied the progressive failure mechanisms of geosynthetic-reinforced column-supported (GRCS) embankment over soft soils by means of finite element (FE) analyses. The emphasis was on the strain-softening behavior of deep cement mixing (DCM) columns. A widely-reported GRCS embankment project was chosen to numerically establish a base model. An advanced Concrete model was incorporated in the FE model, which has proven to be effective in capturing strain-hardening/softening behavior in compression/tension as well as characterizing crack initiation and crack development by numerical comparisons against published laboratory tests. In addition, it was used to identify plastic failure zones and ultimate embankment surcharges, as compared to the conventional Mohr-Coulomb (MC) failure criterion with tension cut-off for embankments.

The development of stress paths, internal forces, and cracks as well as plastic failure zones due to strain softening behaviour was discussed in relation to the progressive failure mechanisms. Numerical results from the base case showed that the failure of the GRCS embankment progresses from side columns in bending to central columns in shearing. The strain-softening initiated by cracks leads to reductions in both bending moment and internal force for the columns in the compression-induced shear zone, with only a reduction in bending moment for the columns in the bending-tension zone.

An extensive parametric study was further performed to examine the role of columns and geosynthetics on progressive failure mechanisms. Investigation of the potential savings in construction by changing the compressive and tensile parameters of columns and tensile stiffness of geosynthetics was then followed. Numerical results showed that a reasonable combination of tensile and compressive parameters of columns as well as tensile stiffness of geosynthetics can prevent the failure of columns and enhance the ability to resist surcharge loads in both bending and shear zones. Besides, it would enable more columns to be mobilized to resist sliding failure. On the contrary, overly high tensile and/or compressive parameters of columns, as well as high tensile stiffness of geosynthetics, would likely result in local failure, and that is a less favorable approach to improving bearing capacity. Overall, this study has provided great insights into the soft ground improvement design for embankments. The outcome of the study would assist design engineers in decision-making, thus optimizing the design performance based on this research.

CRediT authorship contribution statement

Chen Feng: Data curation, Software, Visualization, Writing – original draft. **Shiau Jim:** Writing – review & editing. **Dias Daniel:** Writing – review & editing. **Huang Jianhua:** Funding acquisition, Project administration, Supervision. **Lai Fengwen:** Methodology, Writing – review & editing, Data curation, Formal analysis. **Wang Heng:** Investigation, Methodology, Software, Visualization, Writing – original draft.

Declaration of Competing Interest

The authors declare that they have no known competing financial interests or personal relationships that could have appeared to influence the work reported in this paper.

Data Availability

Data will be made available on request.

Acknowledgements

The financial support from the National Science Foundation of China (Grant Nos. 51678153), the Natural Science Foundation of Fujian Province (2021J011064, 2022J05186) and the Scientific Research Starting Foundation of Fujian University of Technology (GY-Z20093) are gratefully acknowledged.

Appendix A. Comparison of 2D and 3D models

To verify the effectiveness and feasibility of the “equivalent area method” under plain strain conditions, the difference between 2D and 3D numerical results are comprehensively compared and discussed. For this purpose, a 3D numerical model of the GRCS embankment with a half-embankment slice (slice width = a column spacing, *y*-direction) was established. Except for a column diameter of 0.8 m, the geometric configuration and material parameters as well as the rest details of the 3D model are fully the same as those of the 2D model, as shown in Fig. A1.

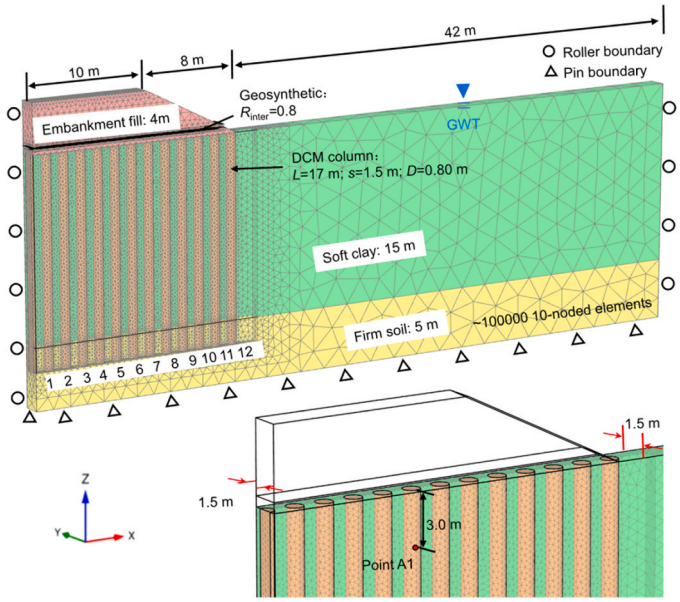

Fig. A1. . Finite elements mesh for 3D numerical modelling.

The stress-strain curves of point A1 (depth equal to 3 m) in column 5 obtained from 2D and 3D models are presented in Fig.A2. It is clear that stress-strain curves in 2D/3D models are in good agreement. Hence, the equivalent area method with an assumption of plain strain conditions only has a slight impact on the constitutive responses of columns (simulated by the Concrete model).

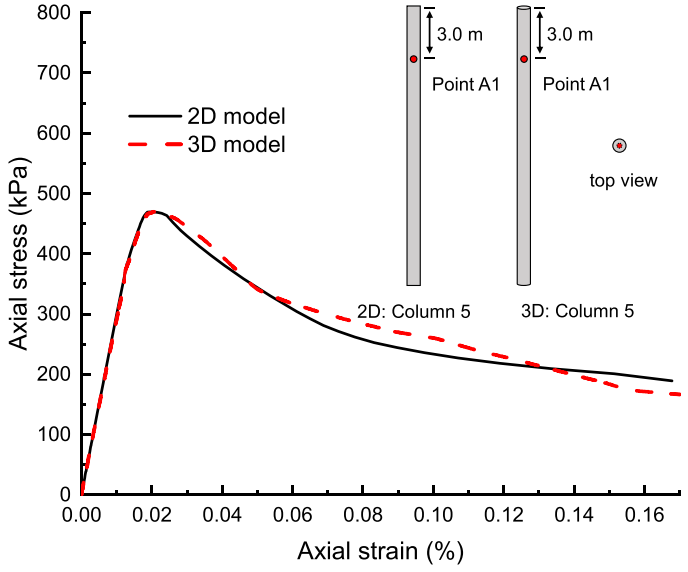

Fig. A2. . Comparison of stress-strain curves of point A1 (at 3 m depth) in column 5.

The comparisons of the internal forces of columns 5 and 12 between 2D/3D models are further presented in Figs. A3 and A4, respectively. Only a very small difference in ultimate surcharge loading (q_{tl}) is observed 3 kPa, with an error lower than 3%. Results in Figs. A3 and A4 show that the distributions of axial force and bending moment in columns 12 and 5 are almost the same. The average errors of axial force and bending moment are both lower than 8% which is in an acceptable range [1,23,46,50]. The higher bending moment in the 2D model indicates that the assumption of plain strain conditions yields the numerical results being on the safe side for a preliminary design.

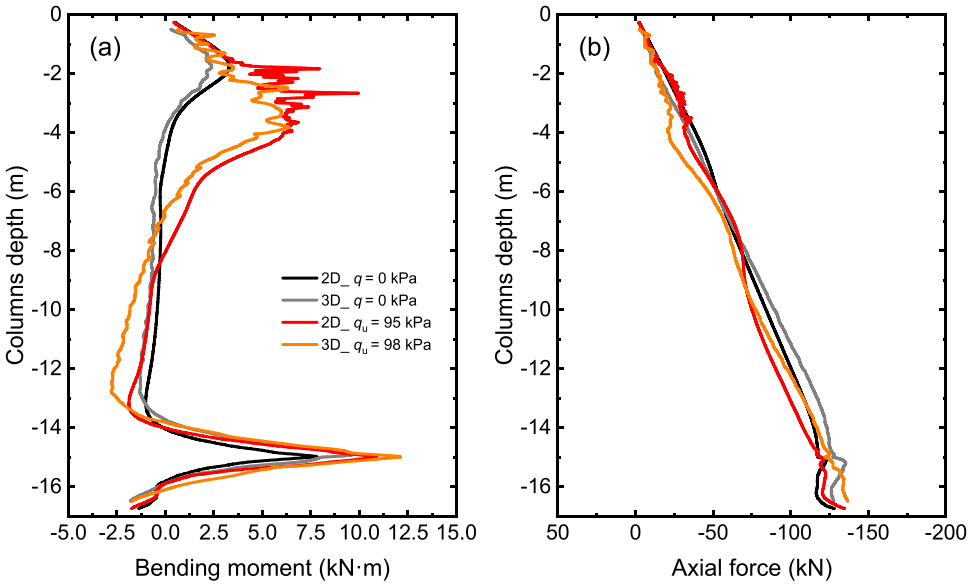

Fig. A3. . Comparison of the internal forces in column 12 between 2D/3D models: (a) bending moment; (b) axial force.

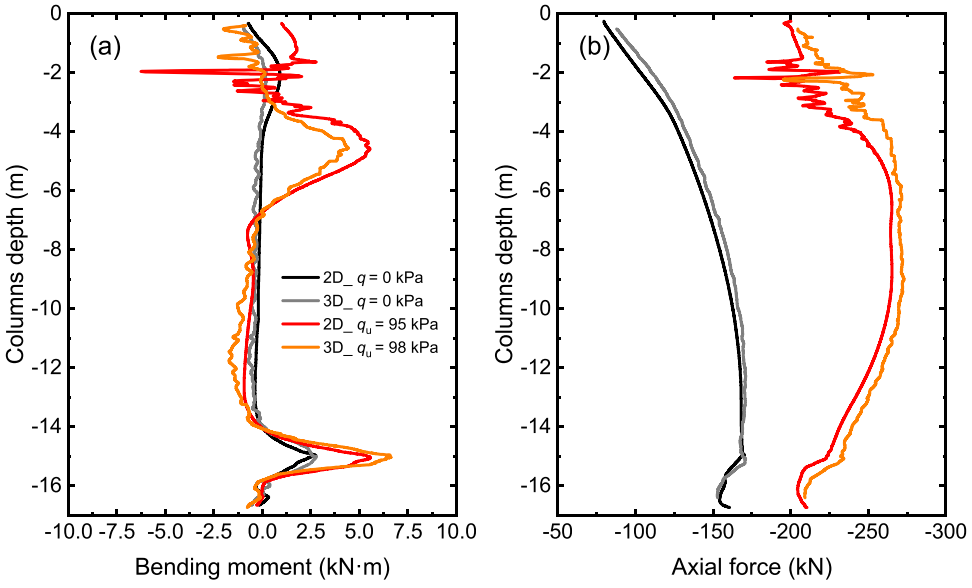

Fig. A4. . Comparison of the internal forces in column 5 between 2D/3D models: (a) bending moment; (b) axial force.

For the GRCS embankment, the intergration of embankment fill, geosynthetic reinforcement, column, and foundation soil respresents a complex soil-structure interaction, the analyses of load transfer among them are of great significance. As a result, the comparison of stresses on them in 2D/3D models is necessary to examine whether the 2D model is available or not. Fig. A5 illustrates the comparison of tensile stresses of geosynthetic reinforcement between 2D/3D models. It can be seen that the tensile stresses obtained from the 2D model are essentially consistent with those from the 3D model. The average error of the tensile stresses between the two models is also lower than 7%. Fig. A6 plots a comparison of vertical stresses on the top of columns supporting the embankment. The average difference in vertical stress calculated from the 2D/3D models is around 9 kPa, with an average error of 6%.

The numerical comparisons have effectively shown that the calculated error generated by simplifying a 3D model into a 2D model is acceptable. Moreover, a trial analysis also shows that, in comparison to a 3D model, the use of a 2D model considerably reduces the computational time. Consequently, this work selects a 2D model with an "equivalent area method" under plain strain conditions, achieving a balance between computational efficiency and accuracy.

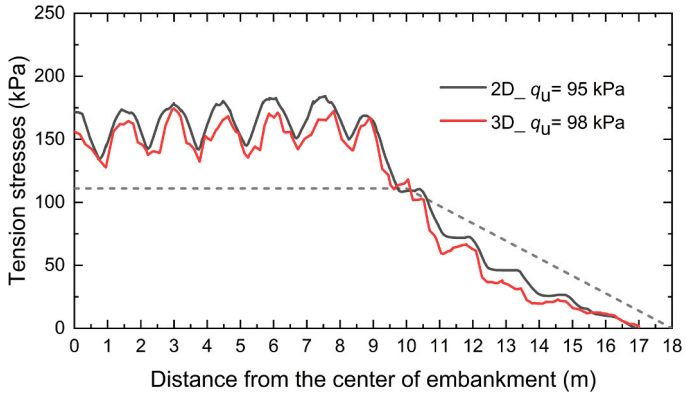

Fig. A5. . Comparison of tensile stress of geosynthetic reinforcement between 2D/3D models.

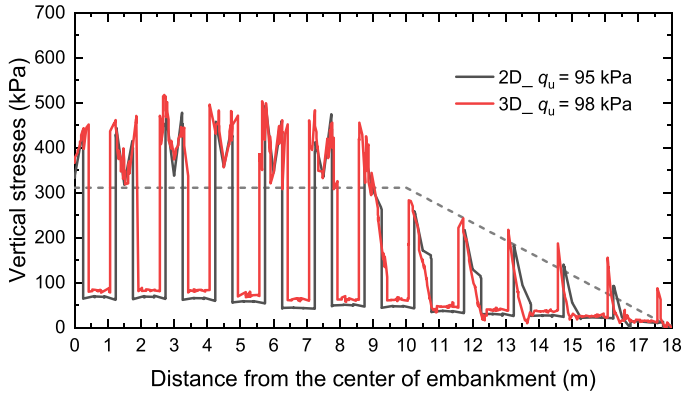

Fig. A6. . Comparison of the vertical stress in composite foundation.

Appendix B. Empirical determination of Concrete model parameters

Table B1 shows the empirical determination of Concrete model parameters relevant to the present study. The time-dependent features are neglected here. Croce et al. [8] suggested that the unit weight of cement-based soil is roughly equal to untreated soil, therefore the mean unit weight of layered soil is recommended here. Constant values of maximum friction angle and maximum dilatancy angle are generally assumed as 30° and 0°. Young's modulus can be determined using $E_{28} = 300\, f_{c,28}$, where the passion ratio of ν is among 0.15 ~ 0.30.

Table B1
Empirical correlations of Concrete model parameters.

Description	Parameter	Unit	Initial parameter value	References
Unit weight	γ	kN/m^3	The weight is roughly equal to untreated soil	Croce et al. [8]
Young's modulus	E_{28}	MPa	$E_{28} = 300 f_{c,28}$	Navin [25]
Poisson's ratio	ν	-	0.15-0.3	Fang et al. [9]
Maximum friction angle	φ_{max}	°	30	-
Maximum dilatancy angle	ψ_{max}	°	0	-
Uniaxial compressive strength	$f_{c,28}$	kPa	$f_{c,28} = 3.46c^{'}$	Kivelö [16]
Normalized initially mobilised strength	f_{con}	-	0.60	Xiao et al. [41]
Normalized failure strength	f_{cfn}	-	0.75	Waichita et al. [39]
Normalized residual strength	f_{cun}	-	0.20	Ta'negonbadi, Noorzad [31]
Compressive fracture energy	$G_{c,28}$	kN/m	$G_{c,28} = 500 G_{t,28}$	Tariq, Maki [32]
Uniaxial plastic failure strain	ε_{cp}^{p}	-	0.003	Terashi [33]
Uniaxial tensile strength	$f_{t,28}$	kPa	$f_{t,28} = 0.15 f_{c,28}$	Navin [25]
Ratio of residual to peak tensile strength	f_{tun}	-	0	-
Tensile fracture energy	$G_{t,28}$	kN/m	0.01	Choosrithong et al. [7]

The standard uniaxial compressive strength ($f_{c,28}$) is obtained by uniaxial compression test for a cured sample after 28 days which is always required in preliminary design. Normalized initially mobilized compressive strength (f_{c0n}), failure strength (f_{cfn}), residual strength (f_{cun}), and uniaxial plastic strain (ε_{cp}^{p}) in compression are all considered as constant values, corresponding to 0.60, 0.75, and 0.20, 0.003, respectively. Compression fracture energy ($G_{c,28}$) is empirically correlated with tension fracture energy ($G_{t,28}$) using a linear relationship of $G_{c,28} = 500 G_{t,28}$, where $G_{t,28}$ is around 0.01. It is conservative that normalized residual tensile strength (f_{tun}) is considered as 0.

Table B1 also presents the correlations between the Concrete model and the MC model. Kivelö [16] reported that the cohesion of cement-based soil in the MC model could be approximately converted with $c^{'} = 0.289\, f_{c,28}$. The rest MC model parameters could be the same as those in the Concrete model. Consequently, once uniaxial compressive strength after 28 days is experimentally determined, a set of Concrete model parameters can be

initially presented empirically (see Table B1). It should be noted that the model parameters determined here are only rough values, which still need to be further calibrated against the available experimental results.

References

[1] Ariyarathne P, Liyanapathirana DS, Leo CJ. Comparison of different two-dimensional idealizations for a geosynthetic-reinforced pile-supported embankment. Int J Geomech 2013;13(6):754–68.
[2] Bergado, D.T. , Long, P. V , 1994. Numerical analysis of embankment on subsiding ground improved by vertical drains and granular piles. *International conference on soil mechanics and foundation engineering*. 1361–1366.
[3] Brinkgreve, R.B.J., Kumarswamy, S., Swolfs, W.M., Foria, F., 2018. PLAXIS 2D Reference Manual Version 2018. Delft: PLAXIS.
[4] British Standards Institution, 2010. Code of Practice for Strengthened/reinforced Soils and Other Fills: BS 8006–1: 2010. BSi.
[5] Chen F, Luo S, Lai F. New analytical solutions for cohesive–frictional soils above deep active trapdoors. Int J Geomech 2022;22(12):04022235.
[6] Chen R-P, Liu Q-W, Wu H-N, Wang H-L, Meng F-Y. Effect of particle shape on the development of 2D soil arching. Comput Geotech 2020;125:103662.
[7] Choosrithong K, Schweiger HF, Marte R. Finite element analysis of mixed-in-place (MIP) columns supporting excavations in slopes considering tension-softening. Can Geotech J 2020;57(6):785–800.
[8] Croce P, Flora A, Modoni G. Jet Grouting: Technology, Design and Control. CRC Press; 2014.
[9] Fang Y-S, Liao J-J, Sze S-C. An empirical strength criterion for jet grouted soilcrete. Eng Geol 1994;37(3–4):285–93.
[10] Guo X, Pham TA, Dias D. Probabilistic analysis of geosynthetic-reinforced and pile-supported embankments. Comput Geotech 2022;142:104595.
[11] Huang J, Han J. 3D coupled mechanical and hydraulic modeling of a geosynthetic-reinforced deep mixed column-supported embankment. Geotextiles Geomembr 2009;27(4):272–80.
[12] Huang J, Han J. Two-dimensional parametric study of geosynthetic-reinforced column-supported embankments by coupled hydraulic and mechanical modeling. Comput Geotech 2010;37(5):638–48.
[13] Huang Z, Ziotopoulou K, Filz GM. 3D numerical limiting case analyses of lateral spreading in a column-supported embankment. J Geotech Geoenviron Eng 2019;145(11):04019096.
[14] Indraratna B, Basack S, Rujikiatkamjorn C. Numerical solution of stone column–improved soft soil considering arching, clogging, and smear effects. J Geotech Geoenviron Eng 2013;139(3):377–94.
[15] Kitazume M, Orano K, Miyajima S. Centrifuge model tests on failure envelope of column type deep mixing method improved ground. Soils Found 2000;40(4):43–55.
[16] Kivelö, M., 1998. Stabilization of embankments on soft soil with lime/cement columns (Doctoral dissertation, Royal Institute of Technology).
[17] Lai F, Chen F, Li D. Bearing capacity characteristics and failure modes of low geosynthetic-reinforced embankments overlying voids. Int J Geomech 2018;18(8):04018085.
[18] Lai F, Chen S, Xue J, Chen F. New analytical solutions for shallow cohesive soils overlying trench voids under various slip surfaces. Transp Geotech 2020;25:100411.
[19] Lai F, Shiau J, Keawsawasvong S, Chen F, Banyong R, Seehavong S. Physics-based and data-driven modeling for stability evaluation of buried structures in natural clays. J Rock Mech Geotech Eng 2022;15(5):1248–62.
[20] Lai F, Zhang N, Liu S, Yang D. A generalised analytical framework for active earth pressure on retaining walls with narrow soil. Géotechnique 2022:1–16.
[21] Lai HJ, Zheng JJ, Cui MJ, Chu J. "Soil arching" for piled embankments: insights from stress redistribution behaviour of DEM modelling. Acta Geotech 2020;15(8):2117–36.
[22] Ma H, Luo Q, Wang T, Jiang H, Lu Q. Numerical stability analysis of piled embankments reinforced with ground beams. Transp Geotech 2021;26:100427.
[23] Meena NK, Nimbalkar S, Fatahi B, Yang G. Effects of soil arching on behavior of pile-supported railway embankment: 2D FEM approach. Comput Geotech 2020;123:103601.
[24] Namikawa T, Koseki J. Experimental determination of softening relations for cement-treated sand. Soils Found 2006;46(4):491–504.
[25] Navin, M.P., 2005. *Stability of embankments founded on soft soil improved with deep-mixing-method columns* (Doctoral dissertation, Virginia Tech).
[26] Nguyen VD, Luo Q, Wang T, Liu K, Zhang L, Nguyen TP. Load transfer in geosynthetic-reinforced piled embankments with a triangular arrangement of piles. J Geotech Geoenviron Eng 2023;149(2):04022131.
[27] Phutthananon C, Jongpradist Pornkasem, Jongpradist Pattaramon, Dias D, Baroth J. Parametric analysis and optimization of T-shaped and conventional deep cement mixing column-supported embankments. Comput Geotech 2020;122:103555.
[28] Rui R, Han J, van Eekelen SJM, Wan Y. Experimental Investigation of Soil-Arching Development in Unreinforced and Geosynthetic-Reinforced Pile-Supported Embankments. J Geotech Geoenviron Eng 2019;145(1):04018103.
[29] Schädlich B, Schweiger H. A new constitutive model for shotcrete. Numer Methods Geotech Eng 2014:103–8.
[30] Schweiger HF, Tschuchnigg F. A numerical study on undrained passive earth pressure. Comput Geotech 2021;140:104441.
[31] Ta'negonbadi B, Noorzad R. Stabilization of clayey soil using lignosulfonate. Transp Geotech 2017;12:45–55.
[32] Tariq KA, Maki T. Mechanical behaviour of cement-treated sand. Constr Build Mater 2014;58:54–63.
[33] Terashi M. Fundamental properties of lime and cement treated soils (2nd report). Rep Port Harb Res Inst 1980:33–57.
[34] Tschuchnigg F, Schweiger HF, Sloan SW. Slope stability analysis by means of finite element limit analysis and finite element strength reduction techniques. Part II: back analyses of a case history. Comput Geotech 2015;70:178–89.
[35] Tschuchnigg F, Schweiger HF. Embankment prediction and back analysis by means of 2D and 3D finite element analyses. Comput Geotech 2018;93:104–14.
[36] Van. In: Eekelen SJM, Brugman MHA, editors. Design Guideline Basal Reinforced Piled Embankments. CRC Press; 2016.
[37] Van Eekelen SJM, Han J. Geosynthetic-reinforced pile-supported embankments: state of the art. Geosynth Int 2020;27(2):112–41.
[38] Venda Oliveira PJ, Pinheiro JLP, Correia AAS. Numerical analysis of an embankment built on soft soil reinforced with deep mixing columns: parametric study. Comput Geotech 2011;38(4):566–76.
[39] Waichita S, Jongpradist P, Schweiger HF. Numerical and experimental investigation of failure of a DCM-wall considering softening behaviour. Comput Geotech 2020;119:103380.
[40] Wang T, Chen W, Li T, Connolly DP, Luo Q, Liu K, et al. Surrogate-assisted uncertainty modeling of embankment settlement. Comput Geotech 2023;159:105498.
[41] Xiao H, Lee FH, Chin KG. Yielding of cement-treated marine clay. Soils Found 2014;54(3):488–501.
[42] Xie M, Li L, Cao W, Zheng J, Dong X. Centrifugal and numerical modeling of embankment widening over soft soils treated by pile-supported geosynthetic-reinforced soil wall. Acta Geotech 2023;18(2):829–41.
[43] Xing H, Zhang Z, Liu H, Wei H. Large-scale tests of pile-supported earth platform with and without geogrid. Geotextiles Geomembr 2014;42(6):586–98.
[44] Xu C, Song S, Han J. Scaled model tests on influence factors of full geosynthetic-reinforced pile-supported embankments. Geosynth Int 2016;23(2):140–53.
[45] Yapage NNS, Liyanapathirana DS. A parametric study of geosynthetic-reinforced column-supported embankments. Geosynth Int 2014;21(3):213–32.
[46] Yapage NNS, Liyanapathirana DS, Kelly RB, Poulos HG, Leo CJ. Numerical modeling of an embankment over soft ground improved with deep cement mixed columns: case history. J Geotech Geoenviron Eng 2014;140(11):04014062.
[47] Yu J, Zhou J, Gong X, Xu R, Li J, Xu S. Centrifuge study on behavior of rigid pile composite foundation under embankment in soft soil. Acta Geotech 2021;16(6):1909–21.
[48] Yu X, Zheng G, Zhou H, Chai J. Influence of geosynthetic reinforcement on the progressive failure of rigid columns under an embankment load. Acta Geotech 2021;16(9):3005–12.
[49] Zaregarizi S, Khosravi M, Coldwell E, Montgomery J. Stochastic slope stability analysis of an embankment supported by isolated soil–cement columns considering spatial variability. J Geotech Geoenviron Eng 2021;147(4):04021009.
[50] Zhang Z, Han J, Ye G. Numerical investigation on factors for deep-seated slope stability of stone column-supported embankments over soft clay. Eng Geol 2014;168:104–13.
[51] Zheng G, Yang X, Zhou H, Chai J. Numerical modeling of progressive failure of rigid piles under embankment load. Can Geotech J 2019;56(1):23–34.
[52] Zhuang Y, Ellis EA. Finite-element analysis of a piled embankment with reinforcement and subsoil. Géotechnique 2016;66(7):596–601.
[53] Zhuang Y, Wang KY. Finite-element analysis of arching in highway piled embankments subjected to moving vehicle loads. Géotechnique 2018;68(10):857–68.